Design and optimization of an electrically driven hybrid Environment Control System

M.P.J. van der Lof

Technische Universiteit Delft

Delft University of Technology

Challenge the future

DESIGN AND OPTIMIZATION OF AN ELECTRICALLY DRIVEN HYBRID ENVIRONMENT CONTROL SYSTEM

by

M.P.J. van der Lof

in partial fulfillment of the requirements for the degree of

Master of Science
in Aerospace Engineering

at the Delft University of Technology,
to be defended publicly on Tuesday July 9, 2024 at 03:00 PM.

Supervisors:	ir. F. Ascione	TU Delft
	Prof. dr. ir. P. Colonna	TU Delft
Thesis committee:	Dr. M. Pini	TU Delft, Chair
	Dr. ir. J.W.R. Peeters	TU Delft, Examiner

An electronic version of this thesis is available at `http://repository.tudelft.nl/`.

PREFACE

Modeling is a discipline that has taught me the virtues of patience and attention to detail. No mistake goes unnoticed, and seldom are there clear indications of where one might have gone wrong. However, when the equations are balanced and the model converges, it creates a sense of joy that only an engineer will feel. Is it worth it? Probably not. But as was stated by Paulo Coelho in the Alchemist "When you can't go back, you have to worry only about the best way of moving forward". On a serious note, I have learned immensely throughout this process and am genuinely pleased with the results achieved. Working on this thesis has deepened my appreciation for the field of engineering, especially thermodynamics.

I am very grateful for the dedicated guidance of my daily supervisor Federica Ascione. Her deep knowledge of modeling and thermodynamics and her readiness to assist have been invaluable. On numerous occasions, when I found myself at an impasse, Federica adeptly pinpointed errors in my reasoning or calculations—often in the units of variables—thereby steering me back on course.

I would also like to extend my heartfelt appreciation to the defense committee for their time and efforts in evaluating this thesis. Special thanks go to my official supervisor, Professor P. Colonna, whose enthusiasm for thermodynamics is contagious. Despite our limited interactions, his guidance was instrumental in advancing my thesis.

I would also like to extend my heartfelt thanks to my girlfriend, who has not only supported me greatly, but has also forgiven me (I hope) for the times when my thesis seemed perpetually "almost finished". Moments of despair were met with compassion, love and care, which I do not take for granted.

Additionally, I would like to thank my parents and my brother. To my brother, you have been a great help to relativize the thesis work, and life in general and keep my mind in balance. Some of my best thesis work came shortly after a conversation with you. To my parents, I would like to thank you for your unconditional support throughout the process.

M.P.J. van der Lof
Delft, July 2024

ABSTRACT

The aviation sector significantly contributes to global air pollution anthropogenic climate forcing. Among the various systems within an aircraft, the Environmental Control System (ECS) stands out as the largest consumer of non-propulsive energy, accounting for 3-5% of total power consumption. This significant energy demand necessitates the investigation of new ECS architectures, seeking for more efficient solutions. A novel electrically driven ECS combining the features of the Air Cycle Machine and the Vapor Compression Cycle is presented. The system design is optimized to minimize weight and power consumption for a critical operating condition, i.e., the aircraft is on the ground during a hot and humid day. The optimization framework integrates the thermodynamic cycle, component sizing and detailed high-speed centrifugal compressor design for the refrigerant. A steady-state model of the ECS has been developed using the a-causal modelling language Modelica , and the optimization framework relies on a Python-Modelica interface.

The optimized design of the hybrid ECS demonstrates the potential for improved efficiency with calculated power consumption values ranging between 59 kW and 82 kW per pack. The weight of the hybrid ECS, which consists of the three heat exchangers, ranges from 19 kg to 45 kg. The Pareto front resulting from the optimization shows a trade-off between power consumption and system weight, where a reduction in power consumption corresponds with an increase in system mass.

An optimal design was identified that balances power consumption and system weight effectively, achieving minimal fuel consumption for a typical single-aisle aircraft flight mission. The chosen design operates with a power consumption of 61.2 kW and weighs 29.3 kg. In the case of cruise conditions, the heat exchangers within this optimal ECS were adequately sized and capable of handling the thermal loads effectively. However, the refrigerant compressor was undersized for the required mass flow rate.

To conclude, the Hybrid ECS potentially represents a step forward in enhancing aircraft energy efficiency, aligning with objectives to mitigate aviation impact on air pollution and anthropogenic climate forcing. The integration of an Air Cycle Machine and Vapor Compression Cycle could offer improvements in reducing power consumption and optimizing performance under specific operational conditions.

CONTENTS

Abstract v

List of Figures ix

List of Tables xi

1 Introduction 1

2 State of the Art 3
- 2.1 Conventional ACM ECS 3
  - 2.1.1 Simple cycle 4
  - 2.1.2 Bootstrap cycle. 5
  - 2.1.3 Combined bootstrap/simple cycle and condensing cycle 5
  - 2.1.4 Comparison between ACM 6
- 2.2 More electric aircraft ACM ECS 7
- 2.3 Vapour Compression Cycle ECS. 8
  - 2.3.1 VCC ECS in commercial aircraft 8
  - 2.3.2 State of the art of the VCC-based ECS 10
- 2.4 Hybrid ACS/VCS ECS 10
  - 2.4.1 Parallel hybrid ECS. 10
  - 2.4.2 Series hybrid ECS 11

3 Modeling of the hybrid ECS configuration 13
- 3.1 Hybrid ECS configuration. 13
  - 3.1.1 Ground configuration 14
  - 3.1.2 Cruise configuration 15
  - 3.1.3 Climb/descent configuration 17
- 3.2 Modeling and simulation 17
  - 3.2.1 Modelica modeling language 17
  - 3.2.2 Working fluids 18
  - 3.2.3 Heat exchangers 18
  - 3.2.4 Intake and exit 21
  - 3.2.5 Compressor and turbine 22
- 3.3 TurboSim 22
  - 3.3.1 Scaling principles 22

4 Optimization 27
- 4.1 Optimization problem statement 27
- 4.2 Optimization architecture. 29
- 4.3 Case study 30
- 4.4 Selection of optimal design 31
  - 4.4.1 Fuel consumption 32

5 Results and discussion 35
- 5.1 Thermodynamic cycle 37
- 5.2 Heat exchanger sizing. 38
- 5.3 Refrigerant compressor design 41
- 5.4 Optimal design for minimal fuel consumption 43
- 5.5 Performance at cruise. 45

6 Conclusion 47
- 6.1 Limitations and Recommendations. 48

Bibliography 49

LIST OF FIGURES

2.1 Ideal reverse Brayton cycle [1] 4
2.2 Simple cycle [1] 4
2.3 Bootstrap cycle [1] 5
2.4 Simple bootstrap cycle [1] 5
2.5 Simple bootstrap cycle with high pressure water extraction [1] 6
2.6 Condensing cycle [1] 6
2.7 Non-ideal inverse Rankine Cycle [2] 8
2.8 VCC of a Boeing 707 [3] 9
2.9 Parallel hybrid ECS configuration 11

3.1 Hybrid ECS complete configuration [4] 14
3.2 Hybrid ECS in ground configuration [4] 14
3.3 Hybrid ECS at ground condition in series configuration 15
3.4 Hybrid ECS in cruise configuration [4] 16
3.5 Hybrid ECS at cruise condition in series configuration 16
3.6 Hybrid ECS in transient configuration [4] 17
3.7 Offset strip fin exchanger [5] 19
3.8 Corrugated multi-louver fin exchanger [6] 21
3.9 modified mass flow function Φ' for two different values of the isentropic exponent [7] 24
3.10 Flowchart of TurboSim compressor design [8] 25

4.1 Schematic of the twin-stage compressor [9] 29
4.2 eXtended Design Structure Matrix (XDSM). 30
4.3 Mission profile for an Airbus A320. 33

5.1 Pareto front showing the ECS system weight as a function of the system power consumption. . . . 35
5.2 Optimization results of a VCC-based ECS. Image courtesy by Ascione F. 36
5.3 Pareto front showing the system COP as a function of the system weight. 36
5.4 Relation between power consumption of the individual components (a), VCS compressor compression ratio (b) and ACS compressor compression ratio as a function of the COP. 37
5.5 Correlation between Refrigerant mass flow rate (a), condensation temperature (b) and evaporation temperature (c) as a function of the COP. 38
5.6 Trend of ACM pressure ratio (a) and total ram air pressure drop (b) as a function of COP. 38
5.7 Breakdown of the heat exchangers weight (a) and heat load (b) as a function of COP 39
5.8 Breakdown of cabin air pressure drop after the main heat exchanger and evaporator (a) and refrigerant pressure drop after the condenser and evaporator as a function of COP 39
5.9 Trend of the core dimensions of the main heat exchanger as a function of the system weight: width of the cabin air side cross-section area (a), height (b) and depth of the ram air side cross-section area (c) 40
5.10 Trend of the core dimensions of the evaporator as a function of the system weight: width of the cabin air side cross section area (a), height (b) and depth of the ram air side cross section area (c). 40
5.11 Trends of the core dimensions of the condenser as a function of the system weight: width of the cabin air cross section area (a), height (b) and depth of the ram air cross section area (c). 41
5.12 Trends of the refrigerant compressors pressure ratio (a) and total efficiency of the first (b) and second (c) stage compressor as a function of the system COP 41
5.13 Trends of the refrigerant compressors axial force (a), rotational speed (b) and impeller hub radius (c) as a function of the system COP 42
5.14 Fuel consumption as a function of the total power demand of the ECS. 43

5.15 $T-s$ thermodynamic chart indicating the processes undergone by the cabin air for the optimal ECS design in the case of ground conditions. . . . 44
5.16 Thermodynamic cycle showing the refrigerant stream 44

LIST OF TABLES

2.1 Comparison of different ACM configurations 7

3.1 Assumptions validity for different components [5] 19
3.2 Description and equations of symbols in the compressor formula 23

4.1 Lower and upper bounds of the design variables. 28
4.2 Lower and upper bounds optimization constraints 29
4.3 Ground operating conditions and required cabin conditions calculated using the in-house software DynTherM [10] 31
4.4 Cruise operating conditions and required cabin conditions calculated using the in-house software DynTherM [10] 31
4.5 Cause of fuel consumption for 3 different flight phases 32

5.1 Set of average optimal input parameters of the compressor. 42
5.2 Optimal design point corresponding to the minimum fuel consumption of the ECS at ground conditions. 43
5.3 Operating conditions and system performance of the ECS operating at cruise conditions. 45

Nomenclature

Abbreviations

ACM	Air Cycle Machine
ACS	Air Cycle machine System
APU	Auxiliary Power Unit
BLT	Block Lower Triangulation
COP	Coefficient Of Performance
ECS	Environmental Control System
EoS	Equation of State
ERF	Effective Radiative Force
HEX	Main heat exchanger
NSGA-II	Non-dominated Sorting Genetic Algorithm
NTU	Number of Transfer Units
ODE	Ordinary Differential Equations
pack	Pressurised Air Conditioner Kit
PSFC	Power Specific Fuel Consumption
TSFC	Thrust Specific Fuel Consumption
VCC	Vapour Compression Cycle
VCS	Vapour Compression cycle System
XDSM	eXtended Design Structure Matrix

Symbols

α_2	Absolute flow angle at the inlet of the refrigerant compressor diffuser	
β	Compressor pressure ratio	-
β	Relative flow angle	°
ΔQ	Change in total heat transfer rate	W
ΔT	Change in temperature	K
$\dot{m}$	Mass flow rate	kg /s
$\dot{W}$	Electric power consumption	kW
ϵ	Heat exchanger effectiveness	-

η	Efficiency	-
γ	Specific heat ratio	-
γ_{PV}	Isentropic pressure-volume exponent	-
Ω	Rotational speed	rpm
Φ	Compressor mass flow function	-
Φ'	Modified mass flow function	-
ϕ_{t1}	Swallowing capacity	-
ψ	Loading factor or work coefficient	-
ρ	Density	$\mathrm{kg/m^3}$
σ	Vector containing stage geometry parameters	-
Re	Reynolds number	-
A	Area	$\mathrm{m^2}$
a	Speed of sound	m/s
C	Heat capacity	W/K
$C*$	Heat capacity ratio $\mathrm{C_{min}/C_{max}}$	
D	Depth	m
F	Force	N
g	Graviation acceleration	$\mathrm{m/s^2}$
H	Height	m
h	Specific enthalpy	J/kg
k	Refrigerant compressor shape factor	-
L_1	Main heat exchanger width hot stream	m
L_2	Main heat exchanger width cold stream	m
L_3	Main heat exchanger height	m
M	Mach number	-
M	Mass	kg
n	Number of moles	mol
P	Power	W
p	Pressure	Pa
P_{t}	Total pressure	Pa
q	Total heat transfer rate	W
R	Universal gas constant	J/mol K
R	thermal resistance based on the surface area	W/m
r	Radius	m

T	Temperature	K
Tr	Temperature split	-
U	Velocity	m/s
U	overall heat transfer coefficient	W/m^2
v	Velocity	m/s
W	Weight	kg
W	Width	m
Y	Pressure drop coefficient	-

Subscripts

1st	First stage compressor
2nd	Second stage compressor
cond	Condenser
c	Cold fluid
eva	Evaporator
HEX	Main heat exchanger
h	Hot fluid
h	Hub
is	Isentropic
max	Maximum value
mech	Mechanical
min	Minimum value
m	Motor
P	Power consumption
ref	Refrigerant
sub	Substance
s	Shroud
tot	Total value
tt	Total
t	Total
W	Weight
w	Wall

1

INTRODUCTION

In the transport sector, aviation is one of the main contributors to air pollution and anthropogenic climate forcing. Its impact has dramatically increased over the last few decades. Anthropogenic climate forcing results mostly from CO_2 and NO_X emissions and water vapor. Lee et al. [11] have calculated the Effective Radiative Force (ERF) of aviation at different moments in time based on global aviation fuel use. ERF is the net radiative force after atmospheric temperatures, water vapor, and clouds are adjusted to the new concentration of greenhouse gasses in the atmosphere. The study shows that the ERF of aviation was 80.4 mW/m^2 in 2011, corresponding to 3.5 % of the total net anthropogenic ERF. In 2018 the ERF reached 100.9 mW/m^2, a staggering 25.5 % increase. Besides ERF, aircraft emissions cause air pollution, i.e. low ozone formed by NO_X and soot that imposes health risks [12]. In response to this environmental crisis, the countries of the European Union signed the "Fly the Green Deal" agreement [13]. The goal is to make the European aviation industry climate neutral by 2050 without compromising on growth, as it has economic and societal importance. To reach this goal, a step-change in aircraft design practices is required. The Environmental Control System (ECS) is the largest consumer of non-propulsive power among all auxiliary systems on board of conventional civil aircraft. The ECS is the responsible for cabin air cooling, dehumidification and pressurization. It accounts for approximately 75% of non-propulsive power, or 3-5% of total energy consumption [14]. The conventional ECS is based on the Air Cycle Machine (ACM) technology. It consists of an inverse Rankine Cycle, where the air bled from the main aircraft engine compressor is cooled down to a target pressure and temperature. To comply with the most recent regulations and to meet the goals set in the "Fly the Green Deal" agreement, the aviation industry is moving towards more electric aircraft architectures. In this framework, the partial electrification of the aircraft auxiliary systems has led to the development of novel electrically driven ECS concepts. This thesis proposes a novel ECS configuration, hereinafter indicated as the Hybrid ECS. This unconventional hybrid ECS combines features of the traditional ACM and the Vapour Compression Cycle (VCC). The analysis is carried out developing a numerical model of the system, exploiting the features of the Modelica language. An integrated system design and optimization tool is used to perform the system optimization and find the best trade-off between system thermodynamic performance and system weight. Such approach does not only allow for the thermodynamic analysis of the system performance, but also for the detailed design of the main system components, considering the effect of the working fluid as well. The system is optimized for a critical operating point, namely on a hot and humid day at ground conditions. The research goal is to assess an optimal design of a hybrid ECS for commercial passengers aircraft at ground condition, which can also meet the ECS operating requirement corresponding to the case of aircraft flying at cruise. The following research question will be answered:

- **What is the optimal design of an electrically driven environmental control system operating on a hot humid day with features of both an air cycle machine and vapour compression cycle?**
    - What is the optimal sizing of components?
    - What is are the optimal operating parameters for the thermodynamic cycle?
    - What is the trade-off between system weight and power consumption?
    - What is the effect of system weight and power consumption on fuel consumption for a typical single-aisle aircraft flight mission?

2

STATE OF THE ART

During the 1940's, the increase of aircraft flying speed and thermal load due to cabin air pressurization and the need for improved passengers comfort raised the need for cabin air conditioning. Linnett and Crabtree [15] published a review of the history of the ECS up until 1993. Their review describes the evolution, application and advantages of different refrigeration and pressurization technologies. Aircraft air cooling started in 1944 with the introduction of the Lockheed P-80 turbojet, an American combat jet. One year later, the first commercial aircraft equipped with cabin air pressurization and conditioning system was presented on the market: the Lockheed Constellation. Remarkably, this system uses a three-wheel bootstrap ACM configuration, the same configuration used many years later. Section 2.1 provides a detailed description of this configuration and other conventional bleed-air ACM configurations. An evolution of the conventional bleed-air ACM configuration is the bleedless ACM. This is currently the most recent and efficient ECS configuration and is installed onboard the Boeing 787 Dreamliner. The novelty of the bleed-less ACM stands in the adoption of an electrically driven compressor to compress the environmental air until a target pressure and temperature is reached. In this way, the air is not bled anymore from the main engine compressor, but the outside air is compressed by a variable speed electric compressor. This has a total fuel consumption saving of 1-2% in the case of the Boeing 787 [16]. Section 2.2 illustrates the differences between the bleed-less ACM and the traditional ACM. A different cooling technology is the Vapour Compression cycle System (VCS). The VCS has generally a higher thermodynamic efficiency, but is less often used in commercial aircraft. Section 2.3 gives an overview of the working principle of a VCS and explains why its employment is limited. Finally, novel configurations that combine features of both the ACM and VCS could reintroduce the use of a VCS in commercial aircraft. Section 2.4 shows the current implementation of hybrid ECSs and discusses proposed configurations from open literature.

2.1. CONVENTIONAL ACM ECS

Merzvinskas et al. [1] published a review paper about air conditioning systems for aeronautical applications in 2020, same to what Linnet and Crabtree [15] did in 1993. In their study they both discuss that all large commercial airplanes use an ACM for their ECS, despite their low thermodynamic efficiency. The reason is that weight and proven reliability get priority over the greater thermodynamic efficiency of a VCS. With the exception of the Boeing 787 Dreamliner, all commercial airplanes use bleed-air to power the ACM. The working principle of an ACM is based on the reversed Brayton cycle. Equation 2.1 shows the correlation between temperature and pressure for isentropic compression/expansion, with γ being around 1.4 for air.

$$\frac{T_2}{T_1} = \frac{p_2}{p_1}^{(1-\frac{1}{\gamma})} \tag{2.1}$$

When air is compressed, its temperature increases and vice versa. Hence, compressing the cabin air gives a temperature difference compared to the ambient air, which enables the use of the ambient air as a heat sink. By expanding the air it gets cooled down to the desired temperature. Figure 2.1 shows the ideal thermodynamic reverse Brayton cycle. Different ACM configurations use this thermodynamic cycle in different ways.

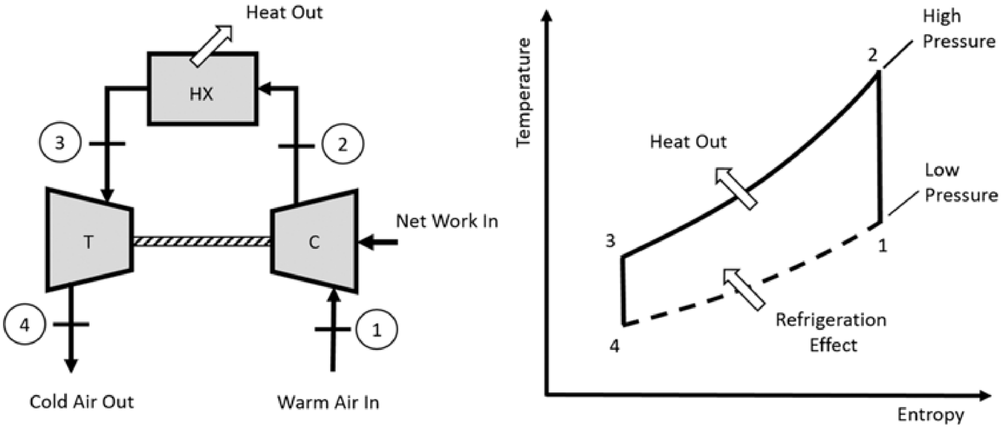

Figure 2.1: Ideal reverse Brayton cycle [1]

Merzvinskas et al. and Linnett and Crabtree have identified four main different ACM configurations. The ACM configurations differ by their different arrangement of the main system components, namely the compressor, heat exchanger, turbine and RAM air fan.

2.1.1. SIMPLE CYCLE

The least complex configuration is the Simple cycle shown in figure 2.2 [1]. The ideal thermodynamic cycle is identical to that of the reversed Brayton cycle shown in figure 2.1 [1]. The air is compressed by the compressor stage of the gas turbine. This air goes through a pre-cooler to keep the temperature within the material limits of the ECS. The majority of the thermal energy gets rejected to the ram air in the main heat exchanger. Finally the air gets expanded and cooled down in the turbine. The ram air duct houses a fan that is driven by the high-speed turbine to ensure enough mass flow at low operating speeds of the aircraft. The fan is often located after the heat exchanger to prevent compression and heating of the ram air before it enters the heat exchanger[17]. The mass flow of the fresh air is regulated by a pressure and a flow control valve. The temperature is regulated by a thermal control valve which allows the fresh air to bypass the heat exchanger and turbine.

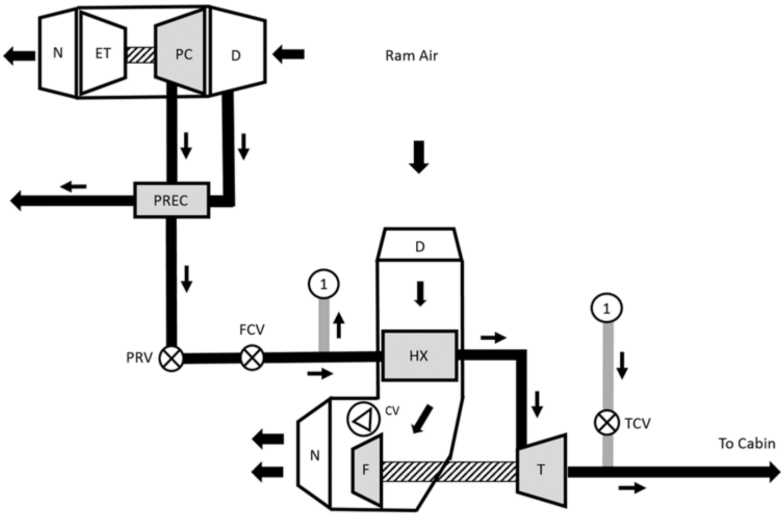

Figure 2.2: Simple cycle [1]

In a non-ideal cycle entropy is generated in all the components, but especially in the compressor and turbine. This translates to a higher work load on the compressor, lower work extraction by the turbine and a higher thermal load on the heat exchanger [18]. This system requires high pressure bleed-air, and thus it is commonly found on military aircraft. The efficiency of this configuration is low because no turbine energy is used to assist in the compression.

2.1.2. BOOTSTRAP CYCLE

The bootstrap cycle adds a compressor that has a common shaft with the turbine, removing the connection between the cooling fan and the turbine. The fan is driven by a separate electric motor. This configuration is shown in fig 2.3 [1]. Thanks to the presence of the ACM compressor (SC), the air can be bled from the main engine compressor at an earlier stage, thus increasing the efficiency of the system when compared with the simple ACM cycle. The downsides are i) a separate cooling fan is needed for low speed operation, ii) the compressor adds complexity to the system.

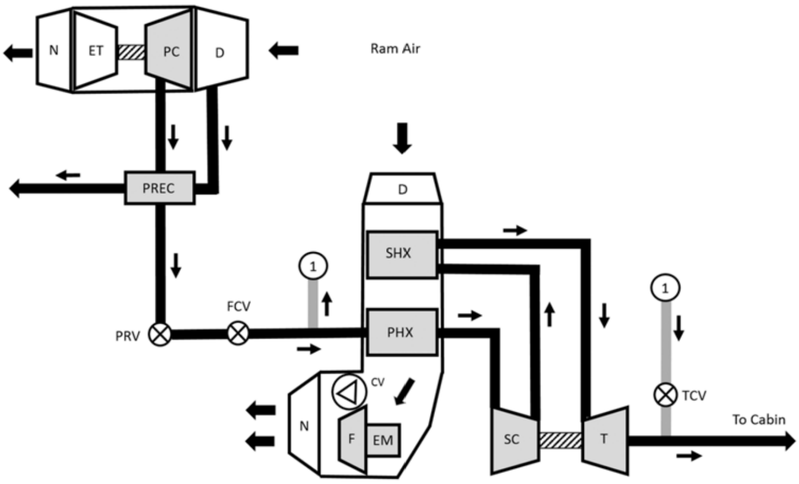

Figure 2.3: Bootstrap cycle [1]

2.1.3. COMBINED BOOTSTRAP/SIMPLE CYCLE AND CONDENSING CYCLE

The combined bootstrap/simple cycle shown in fig 2.4 combines the features of the previous two cycles. Both a fan and a compressor are connected on a common shaft with the turbine. The continuous operation of the fan due to the fixed connection lowers the efficiency compared to the bootstrap cycle, but due to inclusion of a compressor its efficiency is still higher than the simple cycle. By driving the fan directly with the turbine, the need for a separate drive is eliminated. This reduces complexity and maintenance cost.

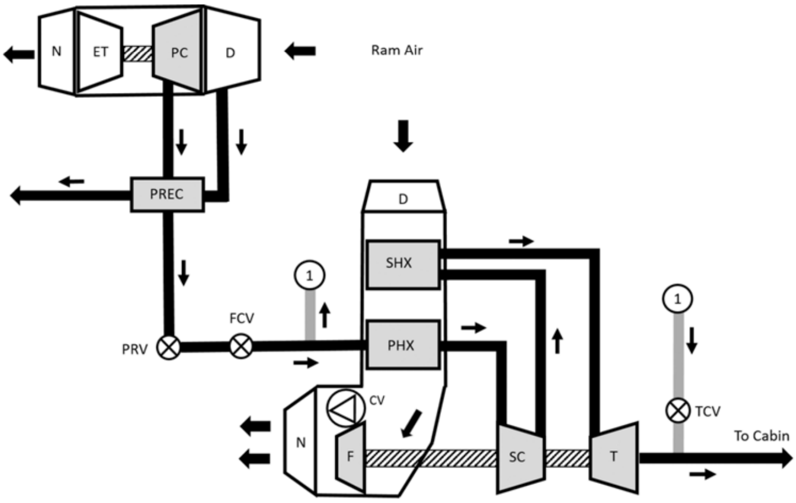

Figure 2.4: Simple bootstrap cycle [1]

During humid conditions the air needs be dehumidified to maintain passenger comfort and to prevent corrosion on the aircraft frame. The before mentioned systems use a coalescing device placed after the turbine outlet to catch water condensate. The temperature of the air stream passing through the coalescing device has to be above freezing temperature to prevent ice formation. The combined simple/bootstrap cycle can be equipped with a high pressure water extractor and reheater. The removal of water at an higher pressure removes the temperature limit after the turbine. The configuration of a combined bootstrap/simple cycle with high pressure water extraction is shown in figure 2.5. Water content from the cabin air is condensed in the condenser (CON). The hot side of the condenser is connected to the reheater (REH) and the cold side is connected the turbine outlet. The water condensate is extracted using an inertial water extractor. The temperature of the dehumidified air is increased in the reheater (REH) before entering the turbine (T). So the task of the reheater is to lower the cabin air temperature before the condenser and increase the cabin air temperature before the turbine. This enables the condensation of water before the turbine without risking condensation within the turbine.

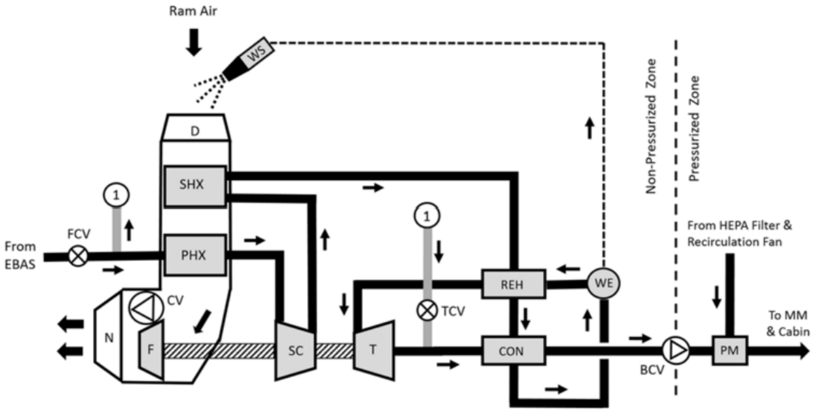
Ram Air
WS
D
SHX
PHX
From EBAS
FCV
1
CV
N
F
SC
T
1
TCV
REH
WE
CON
BCV
PM
Non-Pressurized Zone
Pressurized Zone
From HEPA Filter & Recirculation Fan
To MM & Cabin

Figure 2.5: Simple bootstrap cycle with high pressure water extraction [1]

The condensing cycle shown in fig 2.6 is an evolution of the combined simple/bootstrap that splits the expansion process over two turbines. The purpose of the added turbine is to keep the cold side of the condenser above freezing temperature and to improve the cycle's thermodynamic efficiency by utilizing the latent heat of condensation.

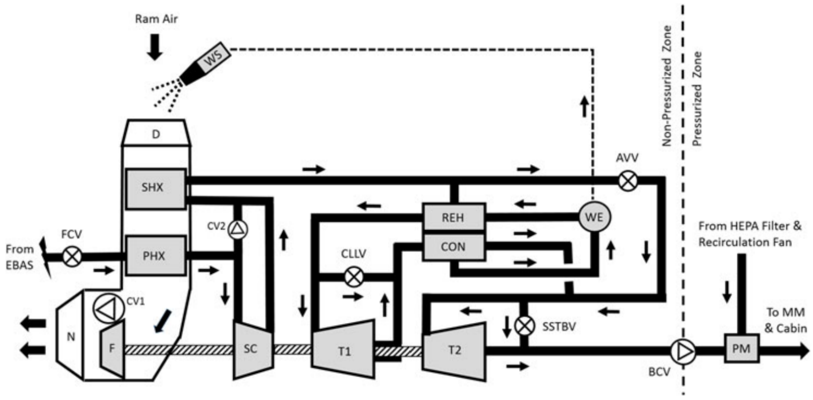
Ram Air
WS
D
SHX
PHX
From EBAS
FCV
CV2
CV1
N
F
SC
T1
T2
CLLV
REH
CON
WE
AVV
SSTBV
BCV
PM
Non-Pressurized Zone
Pressurized Zone
From HEPA Filter & Recirculation Fan
To MM & Cabin

Figure 2.6: Condensing cycle [1]

2.1.4. COMPARISON BETWEEN ACM

The efficiency, weight and complexity differs per configuration. Table 2.1 shows the advantages and disadvantages of the four different configurations. The simple cycle is chosen when a high pressure bleed source is available and low weight and complexity is chosen over efficiency. The bootstrap-cycle has a high efficiency because it does not constantly drive a fan. This configuration does need a separate drive for the fan at ground conditions. The simple/bootstrap cycle eliminates the need for a separate fan drive, which lowers maintenance cost. However, the efficiency is lowered because the fan is constantly pulling power from the shaft. Finally the condensing-cycle improves efficiency over the simple/bootstrap cycle by utilizing the latent heat of condensation. It has the same disadvantage as the simple/bootstrap cycle with the addition of more system components and thus higher complexity.

Table 2.1: Comparison of different ACM configurations

ACM type	Advantages	Disadvantages
Simple-cycle	• Lightweight • Low complexity	• Needs high bleed-air pressure • Wastes turbine work
bootstrap-cycle	• Efficient	• Needs a separate drive for the fan
simple/bootstrap-cycle	• Both fan and compressor are driven by the turbine	• Wastes energy on the fan during cruise • Lower maintenance cost
condensing-cycle	• More efficient than the simple/bootstrap cycle	• High complexity • Wastes energy on the fan during cruise

2.2. MORE ELECTRIC AIRCRAFT ACM ECS

At cruise, conventional aircraft ACMs bleed air from the main engine compressor stages to obtain pneumatic power. Air off-takes impose a penalty on trust specific fuel consumption (TSFC) by reducing the air available for combustion, and thus thrust. An alternative to the conventional ACM is to convert shaft power into electricity via a generator and use it to drive an electrically driven compressor taking air from the environment. Although this approach also reduces thrust, the electrical ACM offers higher efficiency due to the possibility of varying the pressure ratio to meet cooling demand at non-design conditions. Slingerland and Zandstra[19] conducted a study where they quantified the difference of TSFC between bleed-air and bleedless-air configurations. When taking the same amount of exergy from the shaft as from the air after the HPC, the conventional bleed-air system gives a 3.1% lower TSFC. They concluded that a 10%-25% higher efficiency of an electrical counterpart was necessary to compensate the power loss. They expanded their simulation by including a conventional three wheel bootstrap system. For the electrical ECS an electrically driven compressor was used. The electrical ACM showed a much higher efficiency. This was attributed to the possibility of varying the pressure ratio to the cooling demand at off-design conditions. The conventional ACM can only regulated temperature by bypassing the bootstrapped cycle. As the needed fresh cabin air flow is constant, Energy gets wasted at non-demanding cooling scenario's. The electric ACM reduces TSFC by at least 2% over the complete flight cycle of 2 hours and 45 minutes with 50% recirculated air. Calvalcanti and Andrade [20] used a different modeling approach for the same concept, and also demonstrate a significant fuel saving of almost 3% over the flight cycle of 2 hours and 15 minutes. This justifies an electric approach for the design of the ECS. What has not been taken into account in these studies is the impact of bleed air on the design of the gas turbine, specifically the bypass ratio. Using an electrically driven ECS and de-icing system gives the possibility of employing a bleedless turbine engine design. A bleedless turbine design can result in a higher bypass ratio as pointed out by Faleiro[21], and thus a higher efficiency. A bleedless design can also simplify the design by removing the pressure-line infrastructure. It also makes it easier to find air leaks in the system. Another advantage that Faleiro describes is that an electrically driven ECS gives the freedom the optimize the electric power consumption at different stages of the flight. Currently the sizing of systems is done at the critical conditions. With an electric system that consists out of multiple subsystems, the power consumption can be reduced on certain non critical subsystems to allow the critical subsystem to operate at a higher power consumption. This reduces the size of the generator and associated components.

2.3. VAPOUR COMPRESSION CYCLE ECS

A VCS can be found on small business jets such as the Eclipse 500, Cessna Citation Mustang, Cessna Citation CJ1, Embraer Phenom 100, Embrear Phenom 300 and the Honda Jet [1]. The VCS is currently not used on larger commercial aircraft. This was not always the case, as will be expanded on in section 2.3.1. A VCS uses the VCC, also known as the inverse Rankine cycle, to cool the cabin air. Figure 2.7 [2] shows the thermodynamic cycle of a VCC.

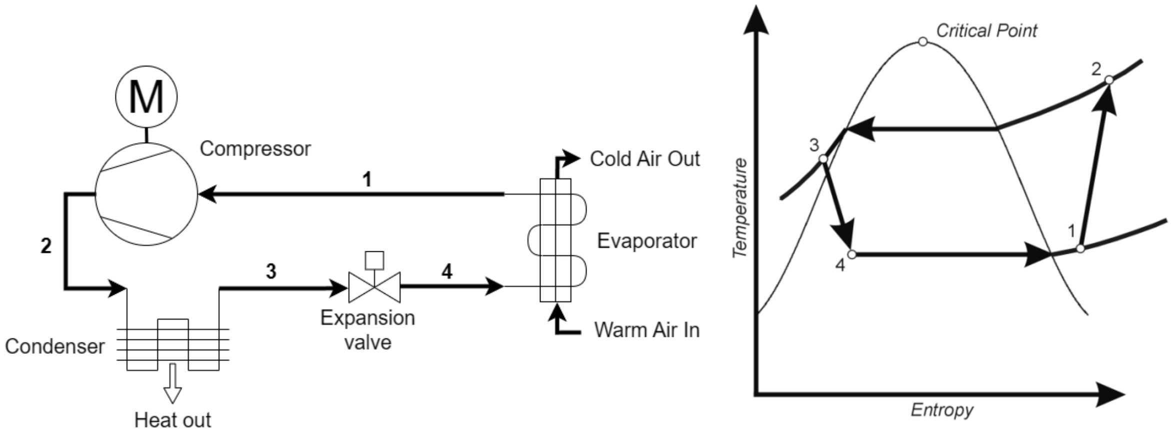

Figure 2.7: Non-ideal inverse Rankine Cycle [2]

At point 1, the refrigerant is in a superheated vapour state. The refrigerant is then compressed between point 1 and 2. upon reaching point 2, the refrigerant enters a condenser and drops in temperature until it starts to condense. During condensation the temperature of the refrigerant stays constant. Once all of the refrigerant is condensed it is subcooled and leaves the condenser and enters the throttling valve at point 3. Between point 3 and 4 the refrigerant expands until it reaches evaporation temperature. At point 4 the refrigerant enters the evaporator. In the evaporator the refrigerant evaporates completely and gets slightly superheated to prevent liquid from entering the compressor. Thermal energy of the cabin air gets transferred to the refrigerant in the evaporator, effectively cooling the cabin air.

2.3.1. VCC ECS IN COMMERCIAL AIRCRAFT

VCSs were used for cabin refrigeration in the 1950's and 1960's. The Boeing 707, 720 [3] and Vickers VC-10 [22] cooled their cabin with a VCS. Figure 2.8 shows the VCS of the Boeing 707.

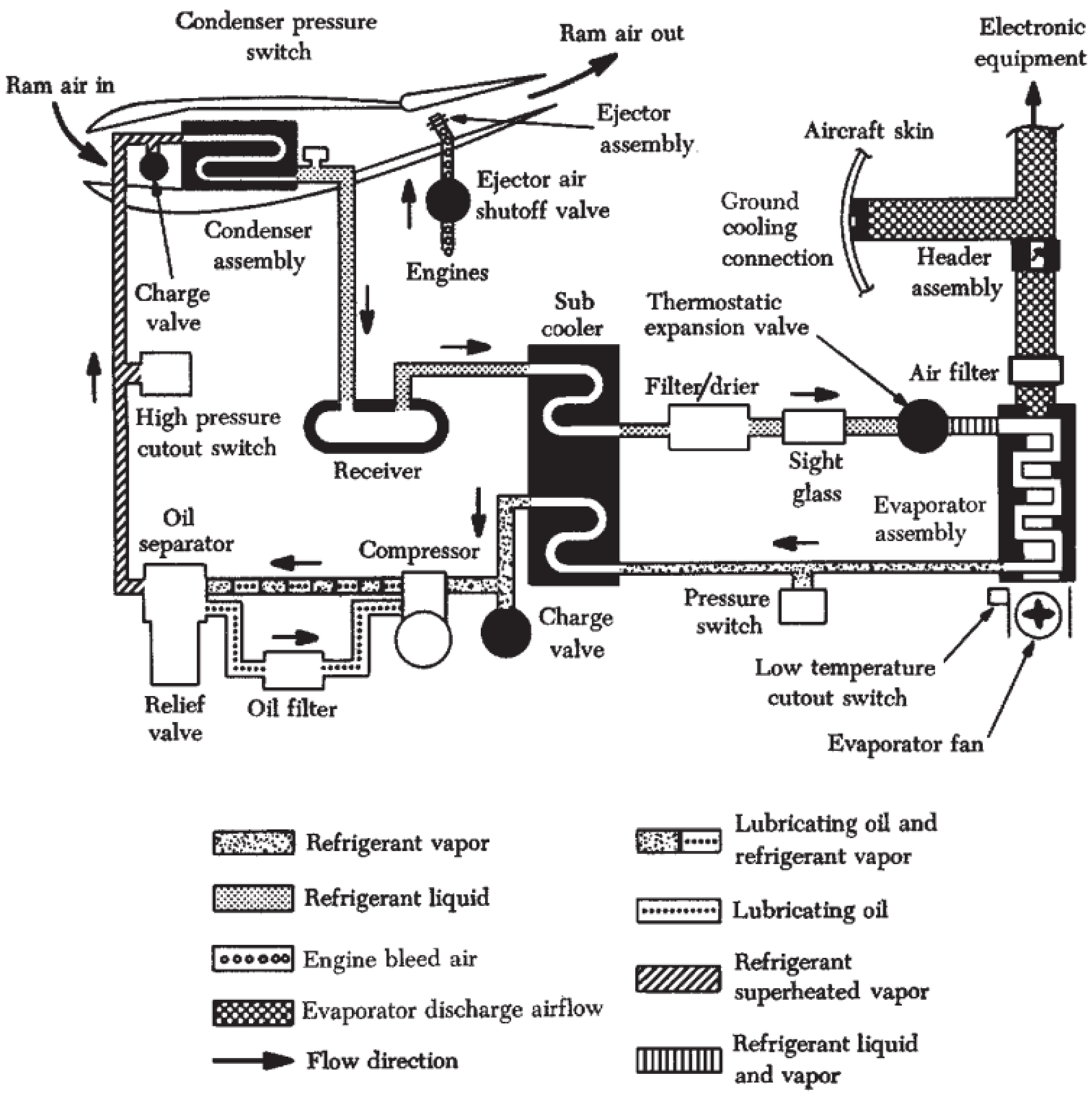
Condenser pressure switch
Ram air out
Electronic equipment
Ram air in
Ejector assembly
Aircraft skin
Ejector air shutoff valve
Ground cooling connection
Header assembly
Condenser assembly
Charge valve
Engines
Sub cooler
Thermostatic expansion valve
Air filter
Filter/drier
High pressure cutout switch
Receiver
Sight glass
Evaporator assembly
Oil separator
Compressor
Charge valve
Pressure switch
Low temperature cutout switch
Relief valve
Oil filter
Evaporator fan
Refrigerant vapor
Refrigerant liquid
Engine bleed air
Evaporator discharge airflow
Flow direction
Lubricating oil and refrigerant vapor
Lubricating oil
Refrigerant superheated vapor
Refrigerant liquid and vapor

Figure 2.8: VCC of a Boeing 707 [3]

This system includes a subcooler that reduces the temperature of the condensed refrigerant below condensation temperature to prevent premature evaporation (flash-off) before reaching the expansion valve to maximise the cooling capacity in the evaporator. The refrigerant used in this system is Freon. Freon is a brand name for refrigerants such and R-22 and R-142b. These refrigerants have been phased out due to their negative effect on the ozone layer [23]. The refrigerant compressor is electrically driven. Oil is added to the refrigerant stream to provide lubrication to the compressor bearings. The cabin air is supplied by a turbocompressor, which uses high pressure bleed air from the sixteenth stage engine compressor. A turbocompressor was used to reduce the flow rate of bleed air from the engine [24] and because of concerns that oil from the engine would contaminate the cabin air if air from the engine compressor was used directly [25]. However, using a turbocompressor is inefficient because useful energy is lost in both the cabin air compressor and the turbine. Although this system was fully developed and operational, it was quickly replaced by an ACM in newer aircraft. Reliability, maintenance and operating limits were the main reasons for phasing out the VCS for newer aircraft. Payne [26] highlights the disadvantages of a VCS in his report where he advocates to use ACMs instead of VCSs for turbine powered commuter aircraft produced in the 1980's. He argues that the ACM is superior in terms of weight, reliability and pulldown capability. The weight of a VCS was mostly heavier because of the use of slow rotating machinery, which speed was limited by brush life in the case of DC power and current frequency in the case of AC power. A number of factors contributed to the lower reliability of a

VCS. Firstly, the refrigerant is at a positive pressure with respect to its surroundings, which results in leakage over time. A VCS is sensitive to the amount of charge [27], thus a leakage degrades the performances. Besides, a leakage of the refrigerant could damage its surrounding components. The second factor for a lower reliability is that the brushes of the DC motors used in the compressor and fan wear down and need to be replaced at regular intervals. His final reason for choosing an ACM over a VCS is the higher pulldown capability of a ACM compared to a VCS designed at the same capacity.

2.3.2. STATE OF THE ART OF THE VCC-BASED ECS

Merzvinskas et al. [1] reported that only executive jets use a VCS. The Coefficient Of Performance (COP) for such VCSs ranges between 3 and 4. Currently, no larger commercial aircraft uses a VCS for cabin cooling. Cavalcanti and Andrade [20] suggest that this comes due to the heavier weight, more difficult maintainability and lack of the industry know-how. However, VCS is used as a supplemental cooling system in the Boeing 787 and Airbus A-380, providing cooling for the galley carts and avionics [28], proving that maintainability and industry know-how are no longer constraints for implementing VCS on commercial aircraft. Furthermore, Saito et al. [29] have proposed a concept that replaces the bleed-less type Air Cycle machine System (ACS) of a 160 passenger aircraft with a VCS. They have found that it is possible to design a VCS at ground operating point that matches the weight of 70 kg of the ACS, while the electric power consumption of the ACS is almost halved. The VCS can match the target weight of the ACS by employing a two-stage centrifugal compressor driven by a high speed motor. Notably, A high speed motor operating at 120,000 rpm weighs only 3.4 kg, which is substantially lighter compared to the 9.8 kg motor rated for the same power used for a screw-type compressor that operates at 9,600 rpm. Thus, the study of Saito et al suggests that weight is not necessarily a limitation either. Facilitating the implementation of VCS on commercial aircraft, new VCS design methods are developed. Ascione et al. [6] have demonstrated the advantages of using an electrically-driven VCC for the aircraft/rotorcraft ECS application. They assessed a novel integrated system design optimization method, taking the thermodynamic cycle, component sizing and working fluid into account simultaneously. The work includes the design of a twin-stage back-to-back compressor using simplified methodology to predict the design and performance of the compressor. This program is called TurboSim [8], this method will be explained in more detail in chapter 3.3. The possibility to implement a VCS in single-aisle short-medium aircraft type is also studied by Liebherr with their Clean Sky Demonstrator D11 [30].

2.4. HYBRID ACS/VCS ECS

The main focus of this study is the hybrid ECS. Here the term hybrid ECS system refers to an ECS system that combines features of both the ACS and VCS. These systems can work in parallel or series. In a parallel configuration, the ACS and VCS work independently from each other. In the case of the two system in series, they are thermally coupled by the cabin air stream.

2.4.1. PARALLEL HYBRID ECS

Parallel hybrid ECS systems are becoming more popular in military aircraft [31]. Agrawal and Mada [32] compare a military parallel hybrid ECS with a conventional ACS and an electric VCS. The parallel hybrid ECS employs a VCS system to cool down the avionics. The conventional bleed air ACS is used to cool the cabin air. This ECS configuration is displayed in Figure 2.9. They conclude that the advantage of this system is that a part of the heat load is handled by the more efficient VCS, while keeping the electrical load within a feasible range.

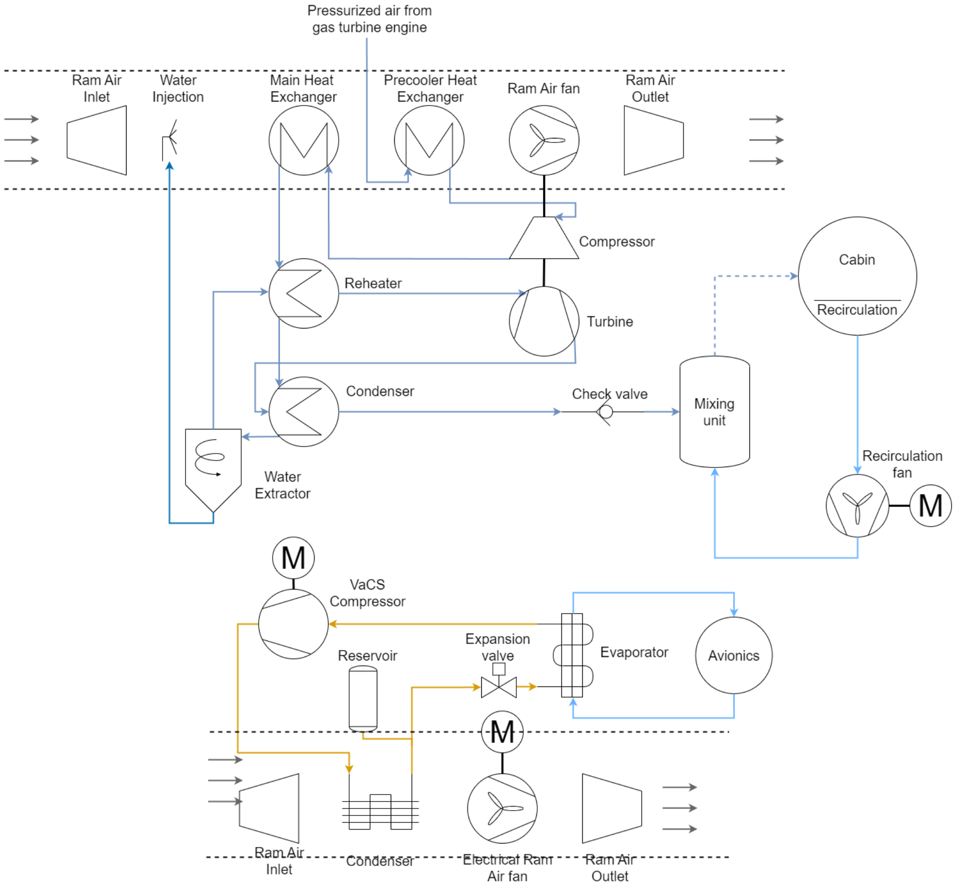
Pressurized air from gas turbine engine
Ram Air Inlet
Water Injection
Main Heat Exchanger
Precooler Heat Exchanger
Ram Air fan
Ram Air Outlet
Compressor
Cabin
Recirculation
Reheater
Turbine
Condenser
Check valve
Mixing unit
Recirculation fan
M
Water Extractor
M
VaCS Compressor
Expansion valve
Reservoir
Evaporator
Avionics
M
Ram Air Inlet
Condenser
Electrical Ram Air fan
Ram Air Outlet

Figure 2.9: Parallel hybrid ECS configuration

An application of parallel hybrid ECS where both the ACS and VCS remove heat from the cabin air is in light turbo prop aircraft. Honeywell has developed a ECS that employs both a VCS and ACS [33]. The VCS provides cooling at ground and low altitude and dehumidifies the air. Honeywell claims that by using a hybrid configuration, the ECS performs better than either system separately, although no performance data is given prove this claim.

2.4.2. SERIES HYBRID ECS

New concepts and numerical optimisations are presented using an ACS and VCS connected in series. These will be discussed in this section. A recent hybrid ECS concept was proposed and patented by Airbus [4]. The patent describes a system that has a cabin air compressor, a two wheel bootstrapped ACS and a VCS using R-134a as the refrigerant. The system has three different operating modes depending on the flight stage. More details about it's operation are given in section 3.1. The system combines the thermodynamic efficiency of a VCS and the proven function and reliability of an ACS. Furthermore, combining an ACS and VCS allows for a reduction in the weight of the evaporator and condenser. The possible reduction of weight and improvement of thermodynamic performance compared to an ACS make this hybrid ECS configuration interesting. Interest in this hybrid ECS configuration is also shown by Liebherr, who is developing a combined ACS/VCS as well. They state that "the combined air cycle and vapour cycle system designs have been solidified. The results were positive and the manufacturing of the demonstrators is underway" [30].

Bender [14] has already examined the thermodynamic properties of this system by analysing the exergy destruction of this electric hybrid ECS using Modelica and compared it to a conventional bleed air driven ECS. His findings were that the electric hybrid ECS provides a potential fuel saving of 66%. There is however a large uncertainty in the contribution of the system weight on the fuel penalty, since the modeling did not involve sizing of the heat exchangers or the design of the refrigerant and cabin air compressors. This thesis addresses this uncertainty by performing an optimization that includes the sizing of components at ground conditions.

3

MODELING OF THE HYBRID ECS CONFIGURATION

This chapter provides an overview of the modeling methodology implemented for the aircraft hybrid ECS, beginning with discussing the three distinct operational modes associated with ground, cruise and climb/descent stages. The configurations for ground and cruise conditions will be examined in more detail as these configurations will be the focus of the modeling effort. The methodology employed for modeling the ECS is discussed from section 3.2 onwards, highlighting the assumptions underlying the model and the most important governing equations. Finally, because the design of the refrigerant compressor is integrated in the system optimization, section 3.3 will detail the principles of the methodology used in the in-house software TurboSim [8] for the compressor design.

3.1. HYBRID ECS CONFIGURATION

The hybrid ECS model is based on a configuration that is proposed and patented by Airbus [4]. Figure 3.1 shows the configuration including all the system components. The system consists of both an ACM, consisting of a compressor (#58) and a turbine (#86), and a VCC, consisting of a evaporator (#30), condenser (#24) and a compressor (#20). The ECS is fully electrically driven and can switch between operation modes by closing and opening valves.

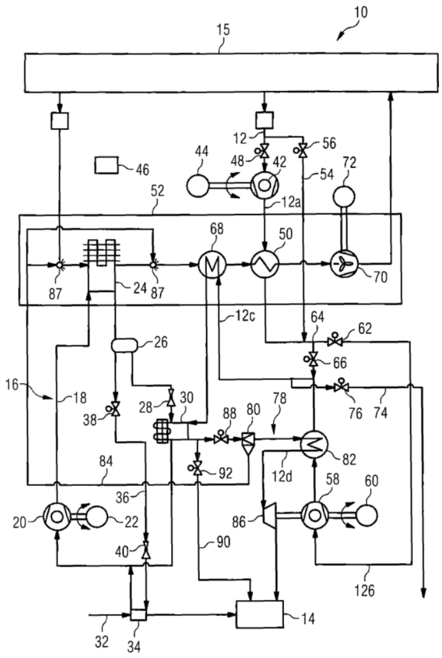
10
15
12
44
48
42
56
46
52
54
72
12a
68
50
70
87
24
87
12c
64
62
26
66
16
18
38
28
30
88
80
78
76
74
84
92
12d
82
58
60
36
20
22
86
90
40
126
14
32
34

Figure 3.1: Hybrid ECS complete configuration [4]

3.1.1. GROUND CONFIGURATION

Figure 3.2 shows the ECS configuration in ground conditions. During ground operation the base compressor (#42) and pre-cooler (#50) are bypassed.

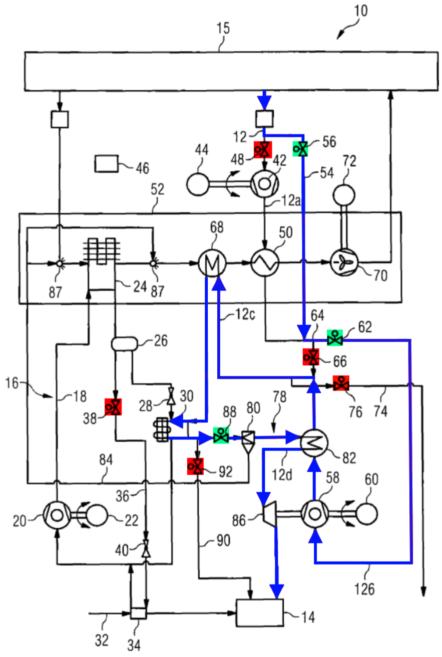
10
15
12
44
48
42
56
46
52
54
72
12a
68
50
70
87
24
87
12c
64
62
26
66
16
18
38
28
30
88
80
78
76
74
84
92
12d
82
58
60
36
20
22
86
90
40
126
14
32
34

Figure 3.2: Hybrid ECS in ground configuration [4]

Figure 3.3 illustrates this specific configuration, including only the components operational at ground level. Fresh air for the cabin is drawn into the ECS at ambient conditions of pressure and temperature. The electrically driven compressor increases the air's pressure and temperature. This is followed by a small reduction in temperature within reheater. The increased temperature from compression facilitates the transfer of heat from the cabin air to the ram air stream via the main heat exchanger. The evaporator further reduces the air's temperature, bringing it below the water vapor's saturation point. The evaporator is coupled to the condenser via the refrigerant stream. The condenser dissipates the heat to the ram air stream. The water from the water-air mixture coming from the condenser get separated under centrifugal force within the high-pressure water extractor. This extracted water is then injected into the ram air stream, increasing the cooling capacity through evaporative cooling. Finally, the dry cabin air from the water extractor is directed to the reheater where the temperature is increased before being expanded in the turbine to the desired pack pressure and temperature.

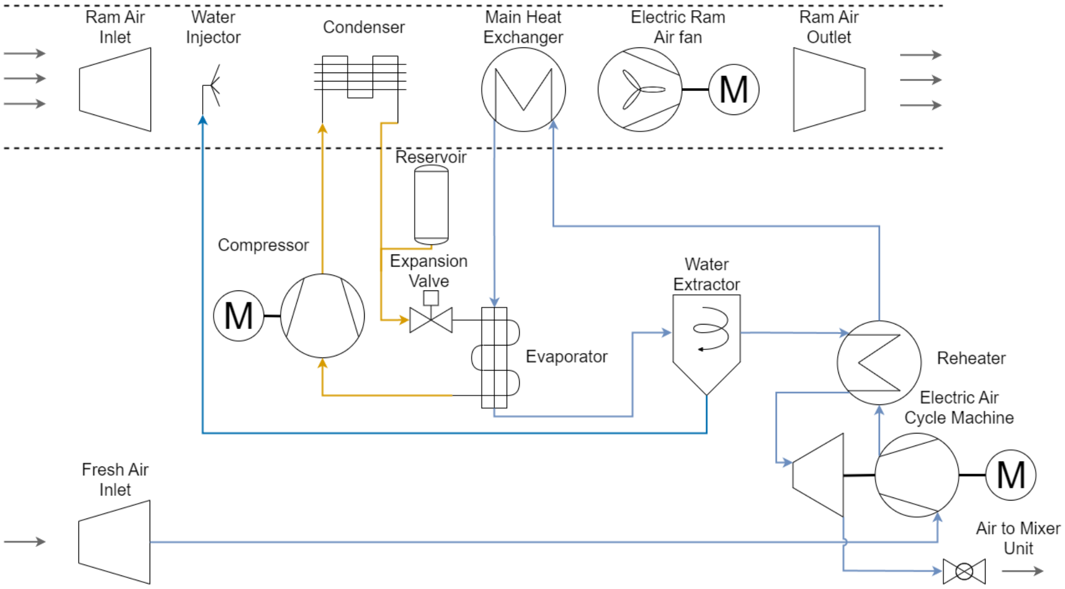
Ram Air Inlet
Water Injector
Condenser
Main Heat Exchanger
Electric Ram Air fan
M
Ram Air Outlet
Reservoir
Compressor
Expansion Valve
M
Water Extractor
Evaporator
Reheater
Electric Air Cycle Machine
M
Fresh Air Inlet
Air to Mixer Unit

Figure 3.3: Hybrid ECS at ground condition in series configuration

3.1.2. CRUISE CONFIGURATION

The air flow in the ECS configuration during cruise conditions is depicted in Figure 3.4. In this configuration the basecompressor (#42) is active and the ACM (#58 and #86) is bypassed.

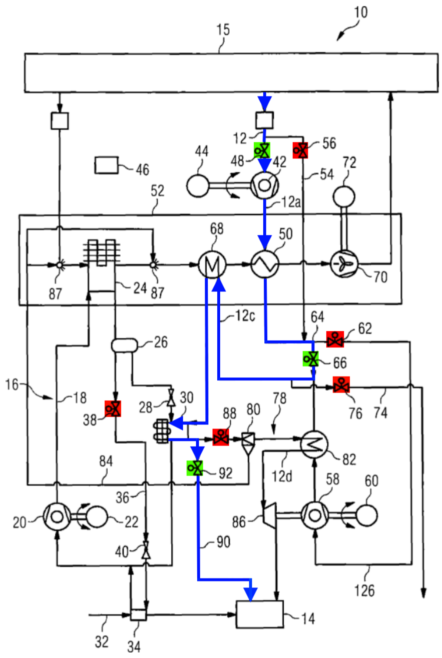
10
15
12
48
42
56
44
54
72
46
52
12a
68
50
70
87
24
87
12c
64
62
26
66
16
18
30
28
88
80
78
76
74
38
84
92
82
12d
58
60
36
20
22
86
40
90
126
14
32
34

Figure 3.4: Hybrid ECS in cruise configuration [4]

Figure 3.5 displays the cruise configuration in more detail. The system features a bleedless configuration. Therefore, the environmental air is compressed by an electrically-driven compressor until the required cabin air pressure. Since in the bleedless configuration, the air temperature is significantly lower than the one in the bleed air configuration, a pre-cooler downstream of the compressor, component #50 in Fig. 3.4, is not necessary. Thus the cabin air flows directly from the basecompressor to the main heat exchanger. Downstream the main heat exchanger, the air is further cooled down by the evaporator to the desired pack temperature. The water extractor is bypassed since the mass fraction of water in the environmental air at cruise conditions is already low.

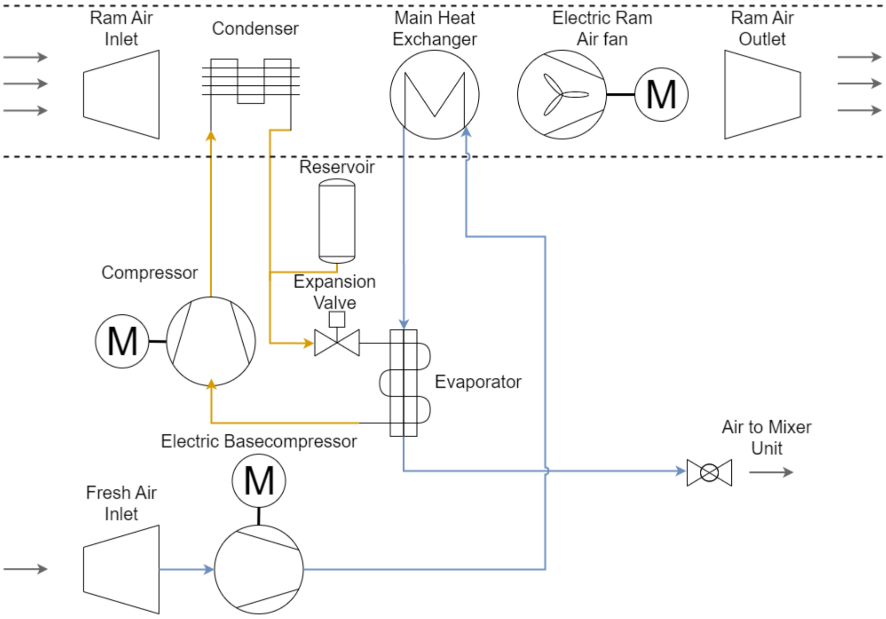
Ram Air Inlet
Condenser
Main Heat Exchanger
Electric Ram Air fan
M
Ram Air Outlet
Reservoir
Compressor
Expansion Valve
M
Evaporator
Air to Mixer Unit
Electric Basecompressor
M
Fresh Air Inlet

Figure 3.5: Hybrid ECS at cruise condition in series configuration

3.1.3. CLIMB/DESCENT CONFIGURATION

During climb and descent the ECS combines the operational characteristics described in section 3.1.1 and 3.1.2. The air is compressed to the desired cabin pressure by the basecompressor (#42). It then follows the same cooling strategy applied to ground conditions. The ECS switches to cruise operation mode once there is no need for dehumidification.

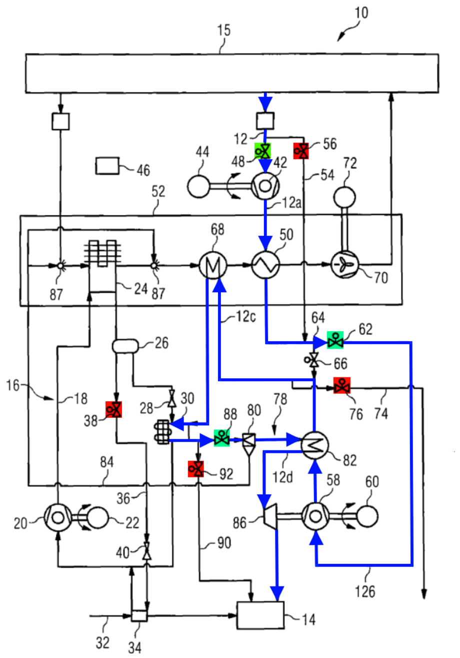

Figure 3.6: Hybrid ECS in transient configuration [4]

3.2. MODELING AND SIMULATION

The behavior of the ECS system is described using mathematical equations. Some of which are based on physics, others on empirical correlations. The simulation of the system is done in the Dymola [34] environment using the Modelica modeling language, section 3.2.1 describes the procedure that Modelica uses to simulate the model. Sections 3.2.2, 3.2.3, 3.2.5 and 3.2.4 describe the fundamental equations and assumptions that govern the behavior of the submodels.

3.2.1. MODELICA MODELING LANGUAGE

Modelica is a high level language that allows the user to describe a system using mathematical relationships and not worry about solving the resulting system of equations. Modelica simulates the system in 6 steps:

1. Transform a structured model into a flat set of equations
2. Structural analysis to verify that the number of equations and variables match and are well posed and perform an index reduction if the system has a index > 1
3. Block Lower Triangular (BLT) decomposition to solve equations explicitly or numerically in the case of implicit equations
4. Code generation for each block from the BLT decomposition
5. Compilation and coupling to an Ordinary Differential Equations ODE solver
6. Simulation

Modelica allows the user to have a focus on the governing equations that capture the phenomena of interest of the model. However, this does not make the user exempt from dealing with resolvability of the model.

The system is sized at constant environmental temperature and pressure. Because the environmental conditions and cooling requirements are constant for the optimization, the ECS can be modelled as a steady state model. The a-causal modelling principle is applied. This allows system component models in Modelica to be connected with each other via effort and flow variables, allowing the use of components from pre-build libraries. Applying this modelling principle to more complex models results in the need to solve (non-linear) implicit equations. To solve implicit equations, it is important to give initial guesses of the variables that are in the vicinity of the solution of the simulation. This is done in Modelica by introducing starting states between the components. These starting states are used as a initial guess for solving the implicit equations. The values for these starting states are calculated based on the design vector using a python script that performs thermodynamic calculations of the ECS. This simplified thermodynamic evaluation is not computationally expensive because pressure drops are not taken into account and the sizes of components do need to be calculated.

3.2.2. WORKING FLUIDS

The model uses two working fluid models to calculate the thermodynamic behavior: a moist air model for the cabin and ram air, and a R134A model for the refrigerant steam. The moist air model is based on the following two assumptions:

- The distance between gas molecules is big enough so that they do not experience mutual interaction and the perfect gas law can applies

- The volume of water in the liquid state is neglected, i.e. the volume of water condensate in the condenser is neglected

These assumptions allow the air model to be modeled using the ideal gas law. The air model is valid for temperatures ranging from 190 K to 647 K and pressures around atmospheric pressure or lower, although a few bars higher is still acceptable. The ideal gas law that governs the Equation of State (EoS) is given as:

$$P = R_{\text{subs}}\rho T \tag{3.1}$$

With R_{subs} being the universal gas constant multiplied by the number of moles per mass of the specific substance:

$$R_{subs} = \frac{Rn}{M} \tag{3.2}$$

To obtain the thermodynamic EoS of the gas the heat capacity C_p needs to be known. The heat capacity is dependant on the substance and temperature. In the moist air model the heat capacity is a combination of the heat capacity of steam and air. The heat capacities of steam and air are given by the NASA polynomials [35], which is data expressed as least-squares coefficients to a seven-term function based on experimental data.

The refrigerant model assumes that the thermodynamic behavior of the refrigerant adheres to empirical measurements. These measurements are pressure, density, temperature, speed of sound, heat capacity and vapor pressure. These measurements are fitted with a linear regression analysis and a nonlinear least squares fitting technique. The result is an EoS that represents the experimental data. Typical accuracy's are ±0.05% for density, ±0.02 for the vapor pressure and ±0.5 and ±1% for the heat capacity [36]. In the present work the thermodynamic and transport properties of the fluid are calculated using CoolProp [37].

3.2.3. HEAT EXCHANGERS

The heat exchangers are modeled following the fundamental heat exchanger modeling approach described by Sekulic and Shah [5]. The assumptions outlined in this reference are applied to this model without alteration.

Table 3.1: Assumptions validity for different components [5]

No.	Assumptions	Heat Exchanger	Evaporator	Condenser
1	The heat exchanger operates under steady-state conditions.	×	×	×
2	Heat losses to or from the surroundings are negligible.	×	×	×
3	No thermal energy sources or sinks in the exchanger walls or fluids.	×	×	×
4	The temperature of each fluid is uniform over every cross section.	×	×	×
5	Wall thermal resistance is distributed uniformly, i.e. constant wall thickness and material homogeneity	×	×	×
6	No phase changes in the fluid streams.	×		
7	Longitudinal heat conduction is negligible.	×	×	×
8	The heat transfer coefficients are constant.	×	×	×
9	The specific heat of each fluid is constant.	×		
10	Uniform and constant overall extended surface efficiency.	×	×	×
11	Uniform distribution of heat transfer surface area.	×	×	×
12	Uniform velocity and temperature at the entrance.	×	×	×
13	Uniform fluid flow rate distribution.	×	×	×

The air to air heat exchanger is an offset strip fin exchanger. The geometry used in the model is shown in Fig. 3.7. The heat transfer surface area of the cold side consists out of all surfaces that are swept by the cold fluid, similarly the heat transfer area of the hot side consists out of all the surfaces that are swept by the hot fluid.

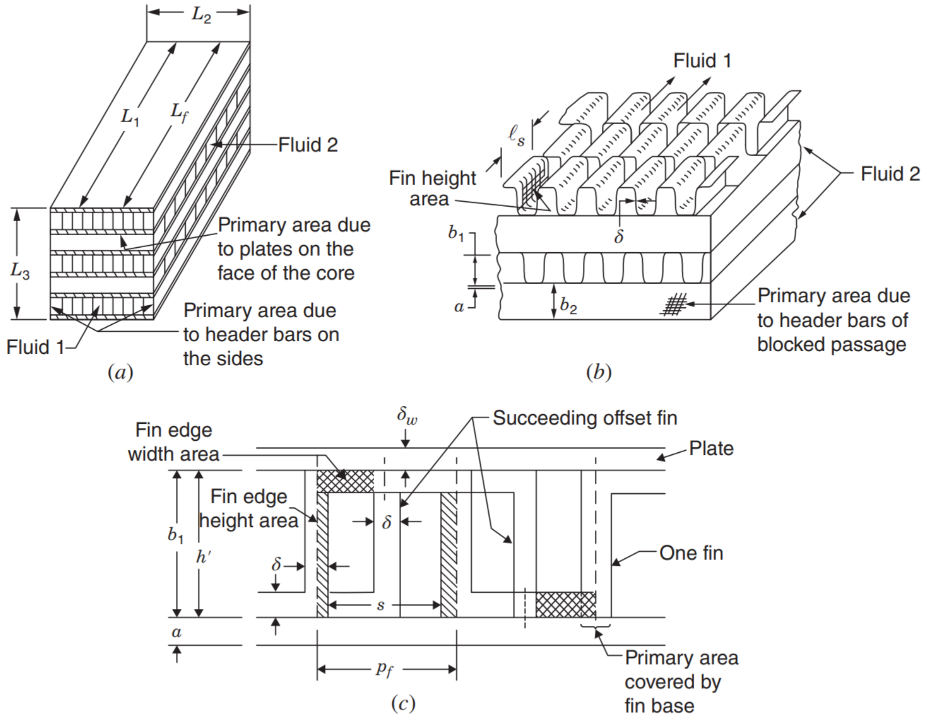
L_2
L_1
L_f
Fluid 2
L_3
Primary area due to plates on the face of the core
Primary area due to header bars on the sides
Fluid 1
(a)
Fluid 1
ℓ_s
Fin height area
Fluid 2
b_1
δ
a
b_2
Primary area due to header bars of blocked passage
(b)
Fin edge width area
δ_w
Succeeding offset fin
Plate
Fin edge height area
b_1
h'
δ
δ
One fin
s
a
p_f
Primary area covered by fin base
(c)

Figure 3.7: Offset strip fin exchanger [5]

The heat exchanger is a 0D model, meaning that only the inlet and outlet conditions are used for computing the heat transfer. The heat exchanger is modeled using the ϵ-NTU method. This methods allows to calculate the heat transfer as a function of the minimum heat capacity C_{min}, maximum temperature difference ΔT_{max} and effectiveness ϵ.

$$q = \epsilon \cdot C_{\text{min}} \cdot \Delta T_{\text{max}} \tag{3.3}$$

Effectiveness is defined as the ratio of the actual heat transfer divided by the maximum possible heat transfer thermodynamically permitted:

$$\epsilon = \frac{q}{q_{\text{max}}} \tag{3.4}$$

Thus the effectiveness is a dimensionless number that indicates the how close a heat exchanger is to the ideal situation. With 0 having no heat transfer and 1 being an ideal heat exchanger. The effectiveness is a function of the heat exchanger geometry, and material and fluid properties. The dependencies can be expressed in three nondimensional groups:

$$\epsilon = \phi\left(\frac{UA}{C_{\text{min}}}, \frac{C_{\text{min}}}{C_{\text{max}}}, \text{flow arrangement}\right) = \phi\left(\text{NTU}, C^*, \text{flow arrangement}\right) \tag{3.5}$$

A heat exchanger is ideal in the case of a heat exchanger with an infinitely large heat transfer surface ($A = \infty$) in a counterflow configuration. When all the assumptions listed in Tab. 3.1 are valid, except for assumption 12 which is optional, the fluid with the smaller heat capacity rate will reach the temperature of the inlet temperature of the other fluid. For heat exchangers of finite size the effectiveness can be calculated if the Number of Transfer Units (NTU), heat capacity ratio C^* and flow arrangement is known, The NTU and flow arrangement are a result of the design of the heat exchanger. The heat capacity ratio is a operating parameter given by the fluids properties. The NTU is also known as the thermal size. From Eqn. 3.5 it can be seen that the NTU is a product of the heat transfer surface area and overall heat transfer coefficient divided by the minimal heat capacity rate. The NTU is not a direct measure for the size of the heat exchanger, as overall heat transfer coefficient and minimal heat capacity rate are also factors in the equation. However, when comparing heat exchangers where U/C_{min} is relatively constant, the NTU depends solely on the heat transfer area and thus does become a measure of the physical size of the heat exchanger. In the $\epsilon - NTU$ method the number of NTU's is calculated by using the relationship between the heat transfer coefficient, area and thermal resistance:

$$UA = \frac{1}{R_{\text{tot}}} \tag{3.6}$$

Where R_{tot} is the thermal resistance of convection in the fluids and conduction in the wall:

$$R_{tot} = R_{\text{c}} + R_{\text{w}} + R_{\text{h}} \tag{3.7}$$

Combining equation 3.5 and 3.6 gives the following expression for the number of NTU's:

$$NTU = \frac{UA}{C_{\text{min}}} = \frac{1}{C_{\text{min}} \cdot R_{tot}} \tag{3.8}$$

The specific equation of the effectiveness of an unmixed cross flow heat exchanger is [38]:

$$\epsilon = 1 - exp\left(C^* NTU^{0.22}\left(exp\left(-C^* NTU^{0.78}\right) - 1\right)\right) \tag{3.9}$$

The order of calculation differs, depending on the design phase. During on-design the required heat transfer, maximum temperature difference and C_{min} is known. Looking at 3.3, the value of ϵ is known as well. Using the definition of NTU given in Eqns. 3.8 and 3.9, the required heat transfer area can be calculated. During off-design the opposite is true. The effectiveness is calculated from the geometry and the total heat transfer is a result of the effectiveness.

The evaporator is a corrugated multi-louver fin exchanger with micro-channel passages for the refrigerant stream. The geometry of this heat exchanger is shown in figure 3.8. The total heat transfer area on the air side is the area swept by the air, minus the frontal area of the edges of the cut louvers. This frontal area is ignored because it makes up a small amount of the total heat transfer area. The heat transfer area on the refrigerant side is area in contact with the refrigerant stream, i.e. the surface area of one micro-channel multiplied by the total number of micro-channels in the evaporator.

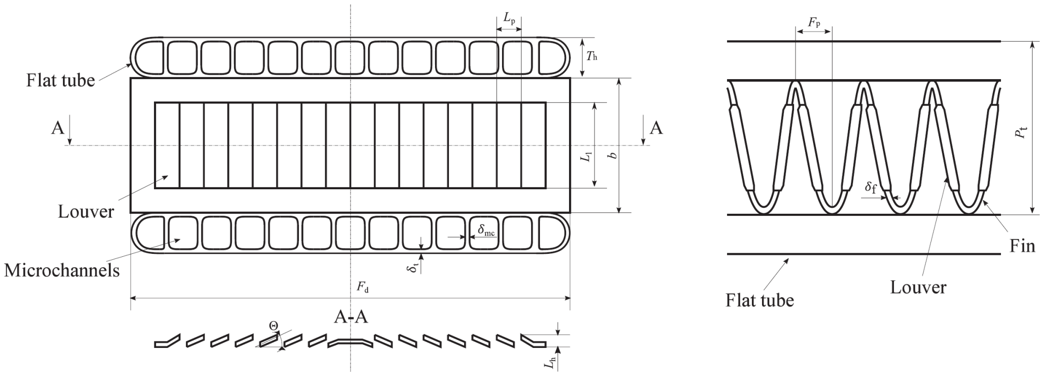

Figure 3.8: Corrugated multi-louver fin exchanger [6]

The evaporator model is split up in two submodels: One submodel addresses superheating, where the refrigerant is entirely in a gaseous state, allowing for the application of the same $\epsilon - NTU$ approach calculation used in the air to air heat exchanger. The other submodel models the evaporation process, where the refrigerant undergoes a phase change and maintains a constant temperature. This requires a different expression than Eqn. 3.9 to calculate the effectiveness. The phase change means that the temperature of the fluid does not increase with an increase of enthalpy. With the heat capacity given as:

$$C = \lim_{\Delta T \to 0} \frac{\Delta Q}{\Delta T} \tag{3.10}$$

Since the increase of temperature of the refrigerant is zero with in a positive heat transfer rate, the heat capacity approaches infinity. This gives a heat capacity rate of approaching infinity. Equation 3.5 shows that the heat capacity ratio C^* approaches zero. This has multiple implications. The first one is that the heat exchanger can be modeled as a counterflow heat exchanger, since there is no temperature gradient in the evaporating fluid. This means that the general expression for efficiency can be used [5]:

$$\epsilon = \frac{1 - \exp[-NTU(1 - C^*)]}{1 - C^* \exp[-NTU(1 - C^*)]} \tag{3.11}$$

The second implication is that since C^* approaches zero the equation can be simplified to:

$$\epsilon = 1 - \exp(-NTU) \tag{3.12}$$

The split of airflow over the models is based on the size of the submodels. The sizing during on-design is based on the required total heat transfer area to reach full evaporation in the evaporation submodel and on the total heat transfer area to reach the prescribed amount of superheating in the superheating submodel.

The condenser has the same geometrical characteristics as the evaporator. However the condenser model consists out of three submodels: a desuperheating, condensing and subcooling submodel. The refrigerant enters the condensing submodel as a saturated vapor and leaves it as a saturated liquid. During condensation the heat capacity rate ratio approaches zero, thus the same procedure for calculating the effectiveness is used as for evaporation in the evaporator. The desuperheating and subcooling submodels are again cross flow heat exchangers without a phase change and follow the same approach as the air to air heat exchanger.

3.2.4. INTAKE AND EXIT

Both the ram air intake and cabin air intake are diffusers that reduce the inlet velocity to a set quantity. This increases the pressure and reduces loses due to pressure drops further in the system. The losses in the diffuser are given by a pressure drop coefficient:

$$Y = \frac{P_{\text{t,in}} - P_{\text{t,out}}}{P_{\text{t,in}} - P_{\text{in}}} \tag{3.13}$$

The ram air exit is a nozzle that recovers the pressure level to the outside environment pressure level. Here the losses are given by the pressure drop coefficient as:

$$Y = \frac{P_{\mathrm{t,in}} - P_{\mathrm{t,out}}}{P_{\mathrm{t,in}} - P_{\mathrm{out}}} \tag{3.14}$$

3.2.5. COMPRESSOR AND TURBINE

The compressor is transferring energy to fluid in the form of a increase in pressure temperature. The internal energy transfer is given by the isentropic efficiency. The total energy transfer from the motor to the compressor takes mechanical losses into account as well. The outlet enthalpy of the compressor is given by:

$$h_{out} = h_{\mathrm{in}} + \frac{h_{\mathrm{out,is}} - h_{\mathrm{in}}}{\eta_{\mathrm{is}}} \tag{3.15}$$

The inlet and isentropic outlet enthalpy is determined by the fluid model and depends on the pressure, enthalpy and mass fraction. The power transferred to the compressor by the motor is given by:

$$P_m = \dot{m}\,\frac{h_{\mathrm{out,is}} - h_{\mathrm{in}}}{\eta_{\mathrm{is}}\,\eta_{\mathrm{mech}}} \tag{3.16}$$

In the case that the compressor is connected to a turbine, the energy balance becomes:

$$P_m = P_{\mathrm{comp}} - P_{\mathrm{turb}} \tag{3.17}$$

The efficiency of the ACM compressor is assumed to be constant. The efficiency of the refrigerant compressors is calculated using the tool TurboSim. See 3.3 for a detailed explanation.

The turbine is connected to the shaft of the air cabin compressor. The power extracted from the fluid by the turbine is given by:

$$h_{out} = h_{\mathrm{in}} - \frac{h_{\mathrm{in}} - h_{\mathrm{out,is}}}{\eta_{\mathrm{is}}} \tag{3.18}$$

Taking mechanical losses into account, the power supplied to the compressor is:

$$P_{turb} = \dot{m}\,(h_{\mathrm{in}} - h_{\mathrm{out}})\,\eta_{\mathrm{mech}} \tag{3.19}$$

3.3. TURBOSIM

The preliminary design of the high-speed twin-stage centrifugal compressor for compressing the refrigerant is performed by utilizing the TurboSim model. Turbosim is a reduced-order model based on scaling principles using a method developed by Giuffre et al. [8]. The method of Giuffre et al. is an extension of the work of Rusch and Casey [7]. Rusch and Casey's research provides a extensive set of design guidelines for large-scale centrifugal compressors, particularly those featuring vaned diffusers and operating with air. Giuffre et al. have extended this framework to create design maps applicable to compressors of varying sizes and operational capacities, especially for handling different fluids. The compressor characteristics calculated by TurboSim are based on the following assumptions:

- The compressor inlet velocity stream is purely axial and uniform
- The use diffuser is vaneless
- The total pressure is close the static pressure

3.3.1. SCALING PRINCIPLES

The performance of a turbomachine can be predicted using dimensional analysis. This is the formal procedure of describing a physical situation using a group of dimensionless variables. This enables the use of experimental relations between variables for a wide range of turbomachinery designs. In TurboSim the compressor characteristics and performance can be expressed as:

$$y = f(\phi_1, \psi, \alpha_2, \beta_{\mathrm{tt1}}, \beta_{\mathrm{tt2}}, \gamma_{PV}, Re, \sigma) \tag{3.20}$$

Table 3.2 describes the compressor variables and gives the equation of the variable where relevant.

Table 3.2: Description and equations of symbols in the compressor formula

Symbol	**Description**	**Equation**
ϕ_{t1}	Swallowing capacity	$\frac{\dot{m}}{\rho_{\mathrm{t1}} \cdot U_2 \cdot D_2^2}$
ψ	Loading factor or work coefficient	$\frac{\Delta h_{\mathrm{tt}}}{U_2^2}$
α_2	Absolute flow angle at the inlet of the diffuser	-
β_{tt}	Compression ratio of the respective stage	$\frac{p_{\mathrm{out}}}{p_{\mathrm{in}}}$
γ_{PV}	Isentropic pressure-volume exponent	$-\frac{v}{P} \cdot \frac{\partial P}{\partial v}\Big\vert_s = -\frac{v}{P} \cdot \frac{c_p}{c_v} \cdot \frac{\partial P}{\partial v}\Big\vert_T$
Re	Reynolds number (indicative of flow regime)	$\frac{\rho v L}{\mu}$
σ	Vector containing stage geometry parameters	-

ϕ_1, ψ and α_2 together describe the inlet and outlet impeller velocity triangle shapes. Conventionally the degree of reaction is chosen to define the ratio between enthalpy rise in the diffuser and the total enthalpy rise, however here α_2 is chosen because it also sets the outlet velocity triangle and it relates directly to the diffuser stability. β indicates together with γ_{PV} the work provided by the impeller.

Together with the mass flow rate and compressor inlet total pressure and temperature, TurboSim designs the compressor. This is an iterative process since the compressor losses are not known beforehand. Firstly the optimal inlet flow angle is set. An optimum inlet blade angle exists which minimizes the relative inlet Mach number. Limiting the relative inlet Mach number is necessary to obtain high efficiencies from high pressure ratio compressors. Setting the optimal inlet angle is done following a well known method to use a modified mass flow function [39]. Rusch and Casey use the same method with a slightly different set of equations using a clearer definition of the relevant non-dimensional parameters [7]. The mass flow function is defined as the mass flow relative to that which can pass through an area of D_2^2 with a gas velocity equal to the inlet total speed of sound with the density at inlet total conditions:

$$\Phi = \frac{\dot{m}}{\rho_{\mathrm{t1}} \cdot a_{\mathrm{t1}} \cdot D_2^2} = \frac{\dot{m}}{\rho_{\mathrm{t1}} \cdot u_2 \cdot D_2^2} \cdot \frac{u_2}{a_{\mathrm{t1}}} = \phi_{\mathrm{t1}} \cdot M_{\mathrm{u2}} \tag{3.21}$$

The goal is to derive a function that allows to minimize the relative inlet Mach number, thus the relative inlet mach number must show up explicitly in the formula. Dixon [39] gives a full derivation to get to a mass flow function that includes the relative mach number. This function is only valid if the axial inlet velocity is purely axial and uniform:

$$\Phi = k \cdot \frac{\pi \cdot M_{\mathrm{w1}}^3}{4 \cdot M_{\mathrm{tu2}}^2} \frac{\sin^2 \beta_{\mathrm{1s}} \cdot \cos \beta_{\mathrm{1s}}}{\left(1 + \frac{\gamma-1}{2} \cdot M_{\mathrm{w1}}^2 \cdot \cos^2 \beta_{\mathrm{1s}}\right)^{\frac{1}{(\gamma-1)+3/2}}} \tag{3.22}$$

After reformulation an expression for a modified mass flow function is given as:

$$\Phi' = \Phi \cdot \frac{4 \cdot M_{\mathrm{u2}}^2}{k \cdot \pi} = \frac{M_{\mathrm{w1}}^3 \cdot \sin^2 \beta_{\mathrm{1s}} \cdot \cos \beta_{\mathrm{1s}}}{\left(1 + \frac{\gamma-1}{2} \cdot M_{\mathrm{w1}}^2 \cdot \cos^2 \beta_{\mathrm{1s}}\right)^{\frac{1}{(\gamma-1)}+3/2}}$$
$$\text{with}$$
$$k = 1 - \left(\frac{r_{\mathrm{1h}}}{r_{\mathrm{1s}}}\right)^2 \tag{3.23}$$

Equation 3.23 shows the gas properties and compressor design parameters explicitly. This enables to plot the modified mass flow function as a function of β at multiple Mach inlet numbers for a specific γ, depending on the fluid. Figure 3.9 shows this modified mass flow function for air ($\gamma = 1.4$) and a high molecular refrigerant gas ($\gamma = 1.2$):

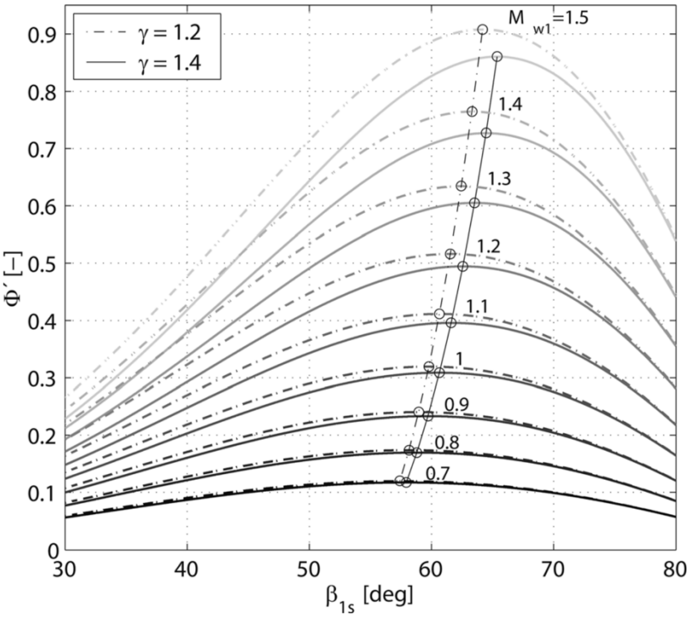

Figure 3.9: modified mass flow function Φ' for two different values of the isentropic exponent [7]

It is clear that for a set Φ' an optimal blade angle β_{1s} exists that minimizes the relative inlet Mach number M_{w1}. In order to set Φ' it is necessary to modify the the second term of equation 3.23 to express Φ' in terms that are either given as input, or that can be calculated from the compressor boundary conditions. Using equation 3.21:

$$\Phi' = \frac{4 \cdot M_{\mathrm{tu2}}^3}{k \cdot \pi} \cdot \phi_{\mathrm{t1}} \tag{3.24}$$

The flow coefficient ϕ_{t1} and impeller shape factor k are given as input parameters. The outlet Mach number M_{tu2} can be calculated using input parameters and assuming isentropic flow:

$$\begin{gathered} M_{\mathrm{tu2}} = \frac{U_2}{a_{\mathrm{t}}} \\ \text{with} \\ U_2 = \sqrt{\frac{\Delta h_{\mathrm{is}}}{\psi}} \\ \text{and } \Delta h_{\mathrm{is}} = f(p_1, \beta) \end{gathered} \tag{3.25}$$

After setting the optimal blade angle at the inlet section, and by using the loading coefficient ψ, diffuser inlet angle α_2 and geometry parameters σ, the initial geometry of the compressor is set. The geometry parameters σ are based on manufacturability limitations. TurboSim then calculates losses at different stations. The pressure ratio based on geometry set by the dimensionless parameters is calculated. If this is lower that the desired pressure ratio, the loading factor is increased and the design process repeats. This process iterates until the desired pressure ratio is met. Figure 3.10 displays the flowchart of the compressor design by TurboSim.

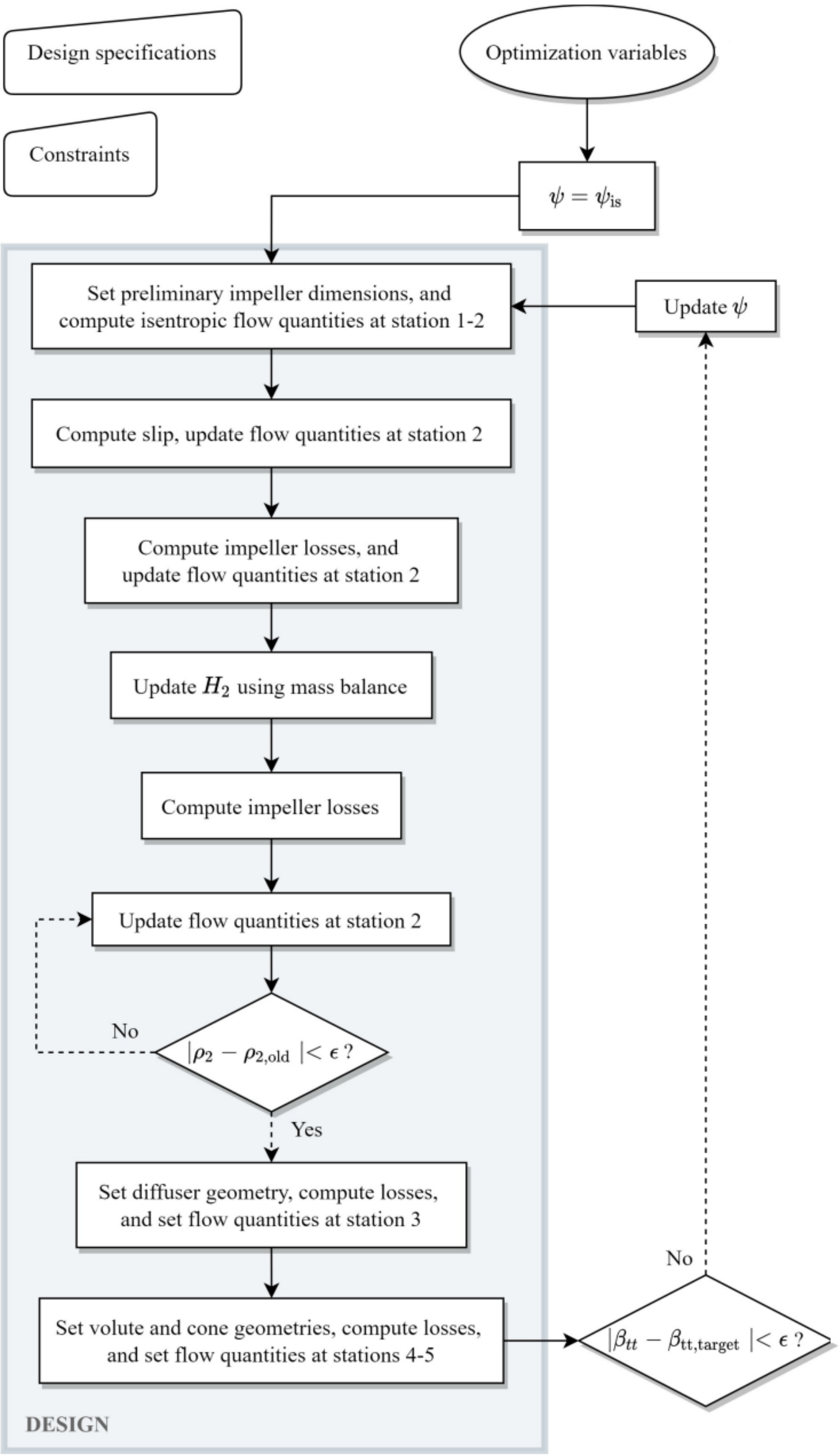
Design specifications
Constraints
Optimization variables
$\psi = \psi_{\text{is}}$
Set preliminary impeller dimensions, and compute isentropic flow quantities at station 1-2
Update ψ
Compute slip, update flow quantities at station 2
Compute impeller losses, and update flow quantities at station 2
Update H_2 using mass balance
Compute impeller losses
Update flow quantities at station 2
No
$|\rho_2 - \rho_{2,\text{old}}| < \epsilon$?
Yes
Set diffuser geometry, compute losses, and set flow quantities at station 3
No
Set volute and cone geometries, compute losses, and set flow quantities at stations 4-5
$|\beta_{tt} - \beta_{\text{tt,target}}| < \epsilon$?
DESIGN

Figure 3.10: Flowchart of TurboSim compressor design [8]

4

OPTIMIZATION

The performance of the hybrid ECS is highly dependent on the sizing of its components and operational parameters. To establish an optimal design and thereby provide a more appropriate reference point for comparison with alternative designs, the system will be optimized at ground operating conditions. In this chapter, the optimization problem, the selection of design variables and the optimization framework are illustrated.

4.1. OPTIMIZATION PROBLEM STATEMENT

The optimization problem can be formalized in the form of:

$$\begin{array}{lll} \min & f_m(x) & m = 1,\ldots,M \\ \text{s.t.} & g_j(x) \leq 0 & j = 1,\ldots,J \\ & x_i^L \leq x_i \leq x_i^U & i = 1,\ldots,N \\ & x \in \Omega & \end{array} \tag{4.1}$$

where $f_m(x)$ is the m-th objective function and $g_j(x)$ the j-th inequality constraint. x_i is the i-th optimization variable with lower bound x_i^L and upper bound x_i^U. The search space Ω consists of solely continuous variables.

The primary aim of this thesis is to design a hybrid ECS conceived to minimize fuel consumption in the case of ground operating conditions. Therefore, the objective function of the optimization is the contemporary minimization of both power consumption and system weight. Since the aircraft velocity at ground level is negligible, the drag caused by the ECS can be disregarded. The ECS power consumption accounts for the energy required for operating the ram air fan, the refrigerant compressors and the ACM power demand, which consists of the power to drive the compressor minus the power generated by the turbine. The analysis focuses on the mass of the heat exchanger components, namely the main heat exchanger, evaporator, and condenser. Formally, the objective functions are given as:

$$\begin{aligned} f_1(x) &= P_{\text{compressor,ACM}} + P_{\text{compressors,refrigerant}} + P_{\text{fan}} \\ f_2(x) &= W_{\text{HEX}} + W_{\text{condenser}} + W_{\text{evaporator}} \end{aligned} \tag{4.2}$$

The weights of the compressors, piping and structural supports are not included in the optimization objectives. Since it is not possible use TurboSim to design a compressor operating with moist air, the problem has been simplified by disregarding the weight of the cabin air compressor and of the turbine. Both the cabin air compressor and the refrigerant compressor are powered by electric motors. The weight of these motors is substantial but constant, and therefore does not vary within the design parameters. Furthermore, variation in the weight of the refrigerant compressor is minor relative to the weight of the heat exchangers. Therefore, the weight of the refrigerant compressor is considered insignificant. Lastly, the detailed design nature of the piping and support structure renders it beyond the scope of this preliminary design.

The design space of the optimization accounts for the geometry of the heat exchangers, the pressure ratio of the ACM, the condensation and evaporation temperature and refrigerant mass flow rate in the VCC and the geometry of the refrigerant compressors. Ideally, all geometrical and operational variables would serve as design variables. However, adopting such an approach incurs high computational costs. Therefore, a selection has been made to include only the geometrical parameters that are most influential to the objective functions. All the operational parameters are included. Table 4.1 shows the bounds of the design vector.

Table 4.1: Lower and upper bounds of the design variables.

Heat exchanger and system design variables			
Description	Symbol	Lower bound	Upper bound
Main HEX width hot stream [m]	L_1	0.1	0.35
Main HEX width cold stream [m]	L_2	0.2	1.1
Evaporator height [m]	H_{eva}	0.25	1.2
Evaporator depth [m]	D_{eva}	0.03	0.16
Condenser height [m]	H_{cond}	0.25	1.3
Condenser depth [m]	D_{cond}	0.04	0.14
Ram air mass flow rate [kg/s]	$\dot{m}_{\text{ram}}$	2.5	3.5
Temperature split main HEX and evaporator [-]	$Tr_{\text{hex,eva}}$	0.2	0.4
Pressure ratio ACM compressor [-]	β_{ACM}	2	3.53
Refrigerant compressors design variables			
Swallowing capacity 1st stage [-]	$\phi_{\text{t1,1st}}$	0.05	0.2
Loading coefficient 1st stage [-]	ψ_{1st}	0.6	1.0
Absolute outlet angle 1st stage [°]	$\alpha_{\text{2,1st}}$	60	75
Diffuser radius ratio 1st stage [-]	$\frac{R3}{R2}_{\text{1st}}$	1.2	1.8
Shape factor 1st stage [-]	κ_{1st}	0.65	0.95
Pressure ratio 1st stage [-]	$\beta_{\text{VCS,1st}}$	1.5	3.5
Swallowing capacity 2st stage [-]	$\phi_{\text{t1,2nd}}$	0.05	0.2
Absolute outlet angle 2st stage [°]	$\alpha_{\text{2,2nd}}$	60	75
Diffuser radius ratio 2st stage [-]	$\frac{R3}{R2}_{\text{2nd}}$	1.2	1.8
Shape factor 2st stage [-]	κ_{2nd}	0.65	0.95
Pressure ratio 2st stage [-]	$\beta_{\text{VCS,2nd}}$	1.5	3.5
Refrigerant mass flow rate [-]	$\dot{m}_{\text{ref}}$	0.3	0.5

The design optimization problem is subjected to constraints to ensure a feasible solution space. The constraints are based on manufacturing or operational limitations. Table 4.2 depicts the constraints for the hybrid ECS optimization and Fig. 4.1 shows a schematic of the compressor. The heat exchanger sizing constraints limit the maximum volume and weight of the ECS and an indirect limit for the pressure drops is set by imposing minimum dimensions. The power consumption of the ram air fan is limited because i) system designs with a high ram air fan power consumption at ground are undesirable because of the impact on total power consumption, ii) a high ram air fan power consumption at ground conditions can lead to the design of very compact heat exchangers. This could have a negative impact on the pressure drops associated with the ram air stream, since the air flow velocity could be significantly high within the heat exchanger passages. The compressor sizing constraints ensure the manufacturability of the compressor. The inlet Mach number is constrained to minimize losses due to shock waves. The axial load is limited to stay within the limits of the axial bearing. Finally, the rotational speed is constrained to ensure acceptable material stresses created by centrifugal force.

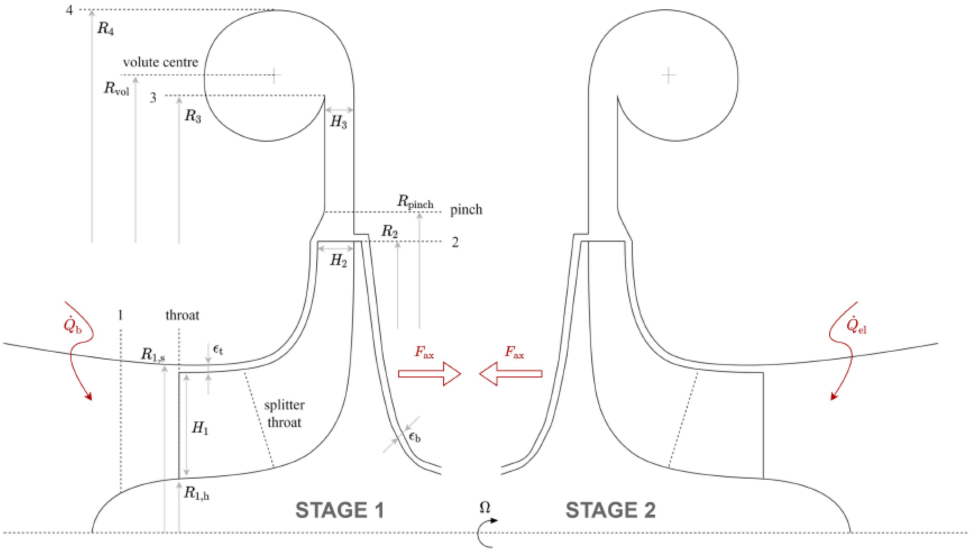

Figure 4.1: Schematic of the twin-stage compressor [9]

Table 4.2: Lower and upper bounds optimization constraints

Heat exchanger and system constraints			
Description	Symbol	Lower bound	Upper bound
Main HEX height [m]	L_3	0.1	1.25
Evaporator width [m]	W_{eva}	0.03	1.25
Condenser width [m]	W_{cond}	0.15	1.25
Ram air fan electric power consumption [W]	P_{fan}	1e1	4e3
Refrigerant compressors constraints			
1st stage refrigerant compressor hub radius [m]	$R_{1,\text{hub,1st}}$	2.5e-3	1e5
1st stage refrigerant compressor impeller height [m]	$H_{2,\text{blade,1st}}$	8e-4	1e5
1st stage refrigerant compressor shroud Mach number [-]	$M_{2,\text{s,1st}}$	-	1.4
1st stage refrigerant compressor outlet Mach number [-]	$M_{2,\text{1st}}$	-	0.7
1st stage refrigerant compressor blade angle [°]	$\beta_{2,\text{blade,1st}}$	-45	-10
2nd stage refrigerant compressor hub radius [m]	$R_{1,\text{hub,2nd}}$	2.5e-3	1e5
2nd stage refrigerant compressor impeller height [m]	$H_{2,\text{blade,2nd}}$	8e-4	1e5
2nd stage refrigerant compressor shroud Mach number [-]	$M_{2,\text{s,2nd}}$	-	1.4
2nd stage refrigerant compressor outlet Mach number [-]	$M_{2,\text{2nd}}$	-	0.7
2nd stage refrigerant compressor blade angle [°]	$\beta_{2,\text{blade,2nd}}$	-45	-10
Refrigerant compressor axial load [N]	F_{axial}	-	1e2
Refrigerant compressor rotational speed [rpm]	Ω	3e4	1.5e5

4.2. OPTIMIZATION ARCHITECTURE

Every design iteration is computationally expensive. Moreover, the exact relationship between the design variables and the objective functions is not known. However, the model is deterministic, ensuring that identical design inputs consistently produce the same outputs. The objective functions can exhibit nonlinear, concave or convex characteristics in relationship to the design vector and can have a few or many local optima. Such challenges necessitate a heuristic approach to solution finding. The optimization employs the Non-dominated Sorting Genetic Algorithm II (NSGA-II) [40]. This is a fast and elitist multi-objective evolutionary algorithm. NSGA-II, being a gradient-free optimizer, is particularly well-suited for computationally intensive problems. Additionally, its capability to explore the entire design space enhances the probability of identifying a global optimum. The optimizer defines the values of the variables in the population at every new generation. The designs that have to lowest values of the objective functions survive. Some variables of the individuals are mutated to explore new solutions. Figure 4.2 illustrates the eXtended Design Structure Matrix (XDSM), which shows the calculation sequence and data dependencies among the various software tools to calculate the objective functions. The optimizer sets the values of the design variables for every generation. The result is a vector that contains the design of all individual designs in the generation. This allows for the use of parallel computing. For every individual design, a simplified evaluation of the thermodynamic cycle of the ECS is performed to calculate the reduced pressure and temperature. Utilizing this output combined with the design variables set by the optimizer, The tool TurboSim designs an optimal twin-stage compressor. The outcome is the actual pressure ratio and the efficiencies of the refrigerant compressors. This outcome forms the input for the Modelica model, together with the system design variables. This model is accessed through the Dymola-Python interface, which creates an instance of Dymola for every individual. Upon completion and convergence of the simulation, the interface reads the results to retrieve the values of the objective functions.

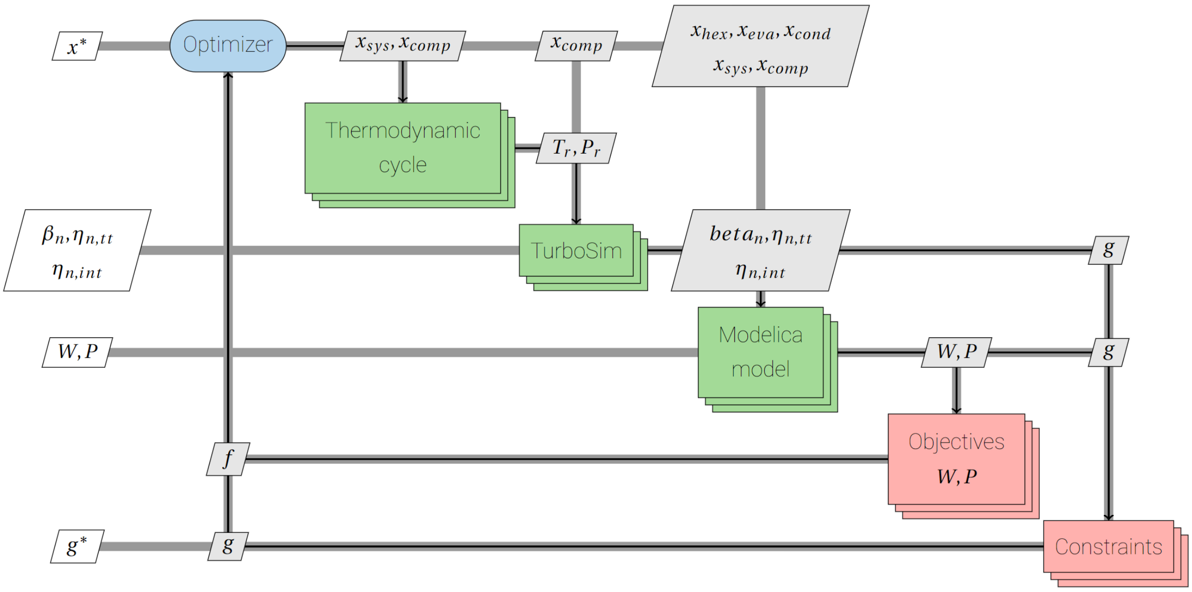

Figure 4.2: eXtended Design Structure Matrix (XDSM).

4.3. CASE STUDY

This section shows the operating conditions of the ECS at both ground and cruise operating points. The environmental conditions and the requirements of the Pressurised Air Conditioner Kit (PACK) outlet vary significantly between these operating points. It is important to note that the requirements here are given for a single pack, a typical single-aisle medium-range aircraft is usually equipped with two packs to ensure proper cooling capacity, even in the case of a failure in one of the packs.

The most demanding operating conditions for the ECS occur on a hot day with high humidity, as it is the most critical operating scenario for the ECS. The specific operating parameters for this case are listed in Tab. 4.3. The cabin air mass flow rate, pack temperature and pack pressure are determined based on the cooling demands and ventilation requirements and calculated using the in-house software DynTherM [10].

Table 4.3: Ground operating conditions and required cabin conditions calculated using the in-house software DynTherM [10]

Description	Value	Unit
ISA +	23	°C
Mach	0	-
Altitude	0	km
Ambient temperature	38	°C
Ambient pressure	101.325	kPa
Water mass fraction	0.009	-
Mass flow fresh cabin air	0.5	kg/s
Temperature pack	-16.2	°C
Pressure pack	102.4	kPa

The operating conditions encountered during the cruise phase provide a comparatively less demanding load on the ECS, yet the necessity to cool the cabin air persists due to the rise in cabin air temperature resulting from compression. This scenario is used to study the performance of the ECS during the cruise phase. The operating conditions are detailed in Tab. 4.4.

Table 4.4: Cruise operating conditions and required cabin conditions calculated using the in-house software DynTherM [10]

Description	Value	Unit
ISA +	0	°C
Mach	0.78	-
Altitude	11.887	km
Ambient temperature	-56.5	°C
Ambient pressure	19.678	kPa
Absolute water fraction	0.00001	-
Mass flow fresh cabin air	0.5	kg/s
Temperature pack	3.4	°C
Pressure pack	76.266	kPa

4.4. SELECTION OF OPTIMAL DESIGN

The result of the optimization is a Pareto front that shows the optimal system designs for a certain combination of weight and power consumption. To select an optimal design, a single figure of merit is needed. Since the overall objective is to minimize the fuel consumption of the aircraft, the fuel consumption stemming from the ECS is chosen as the objective. Scholz [41] presents a methodology to select an optimal system design based on multiple criteria by minimizing the costs, and he presents a method to calculate the fuel consumption of a specific subsystem based on power consumption and weight. This method is used to calculate the fuel consumed by the ECS. For the selection of the optimal system design the following assumptions and simplifications are considered

1. the ECS uses power from the Auxiliary Power Unit (APU) during ground operations, taxiing, take-off and landing;
2. the ECS is running continuously during ground operations, taxiing, take-off and landing;
3. the power consumption of the ECS during cruise operation is assumed to be constant for all the system designs;
4. the lift to drag (L/D) ratio during climb and cruise is assumed to be equal to the L/D ratio during cruise.

Assumption 1 is applied because data about the specific power consumption of a new bleedless engine at idle conditions were not available in the open literature. Without this information, it is not possible to estimate the extra fuel consumption due to a power off-take for the ECS. However, performance characteristics of the Pratt & Whitney APS5000, APU employed in the bleedless Boeing 787, are documented. This allows for the estimation of fuel consumption due to the ECS at ground conditions. Simplification 3 is applied because the ECS is optimized for ground conditions and not for cruise conditions, thus the evaluation of the ECS at cruise is not relevant. This approach is a simplification and for a complete performance evaluation, the system would need to be optimized for the ground, cruise, climb and descent phases.

4.4.1. FUEL CONSUMPTION

The fuel consumption is calculated for 3 flight phases and has 3 different physical causes: i) fuel is consumed directly by the ECS due to its power consumption, ii) fuel is consumed due to the extra weight of the ECS at the cruise and climb/descent phases, iii) fuel is consumed due the extra fuel weight that needs to be carried during flight to operate the ECS after landing. Table 4.5 shows the causes of fuel consumption per flight phase.

Table 4.5: Cause of fuel consumption for 3 different flight phases

Physical cause:	**1: pre-flight**	**2: flight**	**3: post-flight**
Fuel consumption due to power off-take	×		×
Fuel consumption due to the system weight		×	
Fuel consumption due to fuel weight		×	

The fuel consumed due to the power off-take is

$$m_{\text{fuel,i,P}} = P_{\text{ECS}} \cdot t_i \cdot PSFC \tag{4.3}$$

t_i is the duration of the flight phase i and P_{ECS} is the power consumption of the ECS. The power specific fuel consumption ($PSFC$) is based on a P&W APS5000, which is the model of the APU used onboard the Boeing 787. Although the Boeing 787 is larger than the single-aisle aircraft considered in this study, it is currently the only APU in operation that provides electric power only in commercial aircraft. The P&W APS5000 uses 110 kg/h of fuel [42] and provides 450kVA of power [43]. This results in a PSFC of 0.244 kg/kWh.

The fuel consumed due to weight is based on the Breguet Range Equation

$$m_{\text{fuel,i,W}} = m_i \cdot \left(e^{t_i \cdot k_{E,i}} - 1\right), \tag{4.4}$$

the total mass m_i is the mass of the ECS plus the mass of the fuel needed to operate the ECS after landing. $k_{E,i}$ a constant depending on the aircraft and engine design

$$k_{E,i} = TSFC \cdot g \cdot \frac{D}{L}. \tag{4.5}$$

The total fuel consumption is calculated for a typical flight mission of an Airbus A320 with a turnaround time of 45 minutes [44], a total taxi time of 10 minutes and a flight time of 1.8 hours [45]

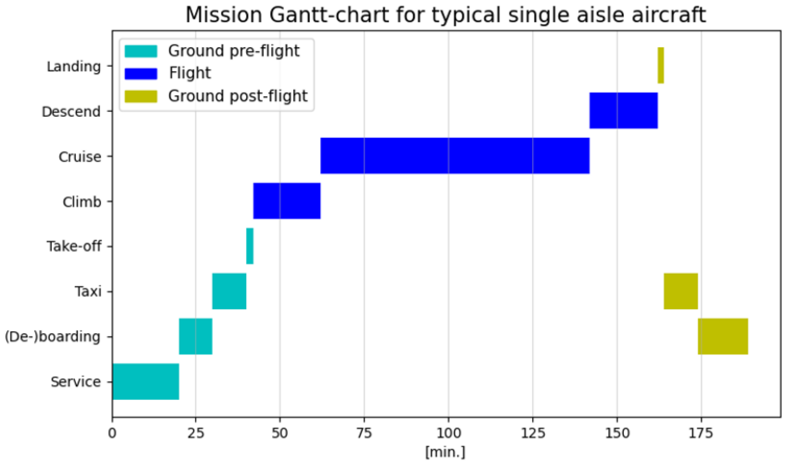

Figure 4.3: Mission profile for an Airbus A320.

5

RESULTS AND DISCUSSION

Figure 5.1 displays the Pareto front of all non-dominated solutions, plotting the power consumption on the horizontal axis and the system weight on the vertical axis. The system weight consists of the weight of the main heat exchanger, evaporator and condenser, which are the components that exhibit the most significant weight variations during optimization. The weight of the compressor has been overlooked, as explained in Ch. 4. The results demonstrate the existence of a trade-off between system weight and power consumption, indicating that the weight increases non-linearly as power consumption decreases.

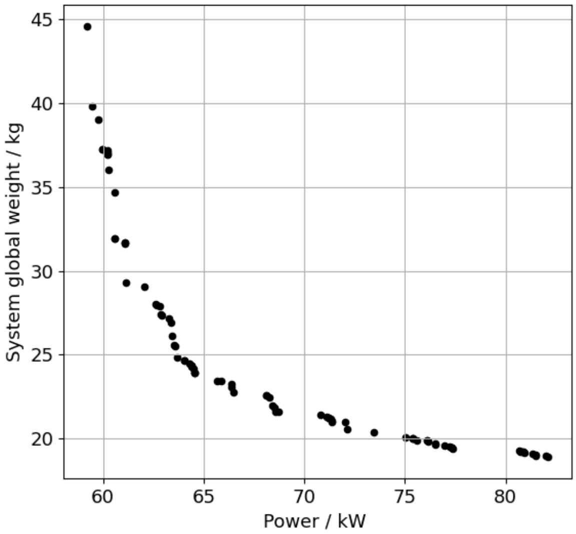

Figure 5.1: Pareto front showing the ECS system weight as a function of the system power consumption.

The performance of the hybrid ECS is compared with the optimization results of a VCC-based ECS. Figure 5.2 shows the weight and power consumption of the VCC-based ECS at ground conditions. The results are not directly comparable as the VCC based ECS was optimized at three different operating points, namely ground, cruise and faulty pack at cruise. Furthermore, since this system was optimized for flight conditions as well, drag was taken into the objective function. Lastly, the weight of the VCC-based ECS includes more components, thus only the power consumption can be used for comparison. Nevertheless, the range of power consumption displayed in Fig 5.2 provides a usable reference, as the cooling load at ground conditions is equal. The power consumption of the VCC-based ECS represents two packs, whereas the the hybrid ECS results represent a single pack. The power consumption of the VCC-based ECS for a single pack is between 100 kW and 125 kW. The power consumption of the hybrid ECS ranges from 60 kW to 82 kW. This suggests that the hybrid ECS could be a more efficient cooling solution, although a multi-point optimization of the hybrid ECS is needed to make this statement conclusive.

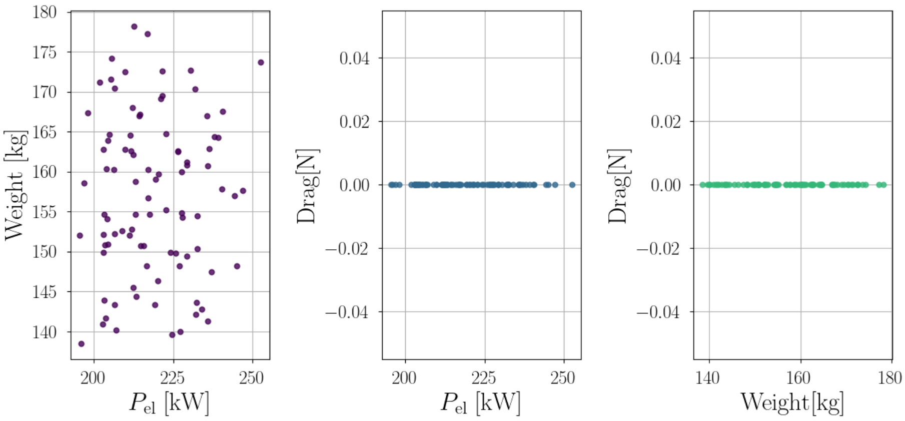

Figure 5.2: Optimization results of a VCC-based ECS. Image courtesy by Ascione F.

Figure 5.3 displays the system COP as a function of the system weight. The COP is defined as

$$\mathrm{COP} = \frac{\dot{m}\cdot(h_{\mathrm{in}} - h_{\mathrm{out}})}{\dot{W}_{\mathrm{compr,ACS}} + \dot{W}_{\mathrm{compr,VCS}} + \dot{W}_{\mathrm{fan}}} \tag{5.1}$$

where h_{in} represents the ECS inlet enthalpy before the ACM compressor, and h_{out} represents the ECS outlet enthalpy after the ACM turbine. The numerator indicates the thermal cooling demand of the ECS, which remains constant throughout the optimization as the inlet and outlet temperature, pressure and mass flow rate of the air are constant. Equation 5.1 is only applicable at ground conditions, where the enthalpy change is primarily associated with a difference in temperature, rather than pressure differences between the outside air and cabin air. As the numerator in Eqn. 5.1 is fixed, the COP is inversely proportional to the system power consumption. Therefore, the COP increases as the power consumption decreases, at the expense of a higher system weight (Fig. 5.3).

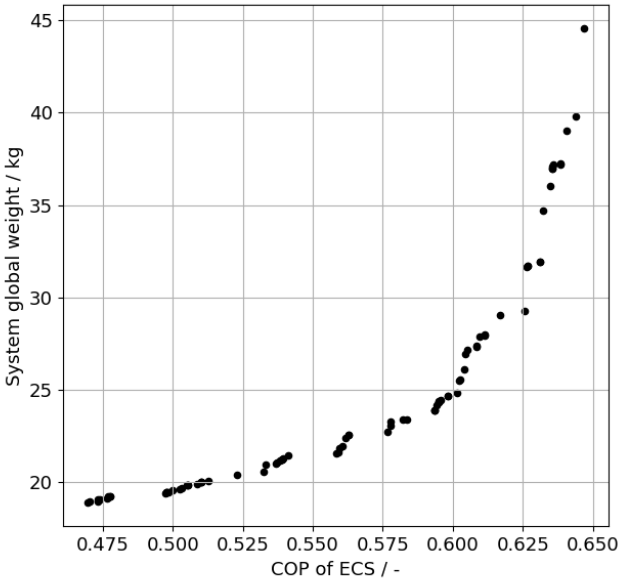

Figure 5.3: Pareto front showing the system COP as a function of the system weight.

5.1. THERMODYNAMIC CYCLE

The heat load and sizing of the heat exchangers depend on the system thermodynamic cycle operating parameters. Specifically, these include the pressure ratio of the ACM compressor, VCS compressor, ram air fan, and the temperature ratio of the two heat exchangers. These parameters determine the inlet temperature and pressure of the heat exchangers and ultimately impact the total power consumption. The power consumptions of the VCS compressor, the net power demand of the ACM and ram air fan electric consumption are shown in Fig. 5.4a. In all the cases, the power consumption decreases as the COP increases. Notably, the ACM, comprising both the compressor and the connected turbine, accounts for the largest share of power consumption. In correspondence of the lowest values of COP, the ram air fan power demand reaches a plateau at 4 kW, which is equal to the maximum allowable value imposed within the optimization constraints.

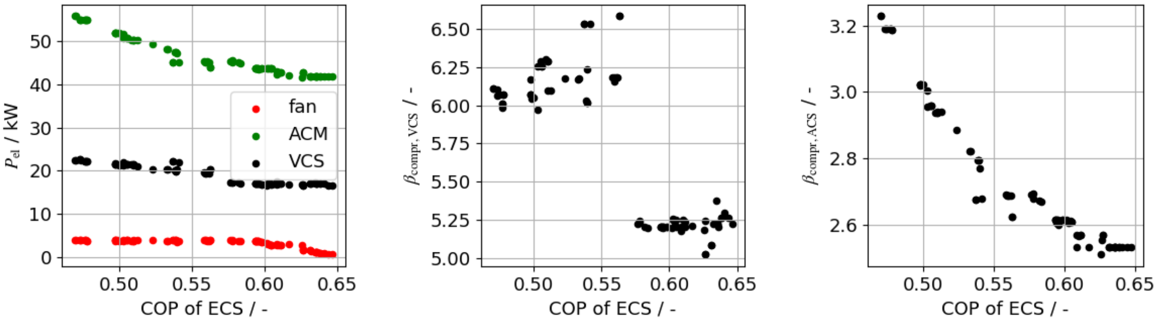

(a) (b) (c)

Figure 5.4: Relation between power consumption of the individual components (a), VCS compressor compression ratio (b) and ACS compressor compression ratio as a function of the COP.

The cabin air mass flow rate is constant, therefore, any variation in the power consumption of the ACS compressor is a direct consequence of changes in the compressor pressure ratio. As illustrated in Fig. 5.4c, the ACM compressor pressure ratio decreases with increasing COP, ranging from a minimum of 2.55 to a maximum of 3.2.

The plateau observed in correspondence of the minimum values of the pressure ratio is associated with the maximum allowable dimensional constraints of the main heat exchanger. In fact, a reduction of the ACM compressor pressure ratio implies a reduction of the temperature at the inlet of the main heat exchanger, and therefore the need for larger heat transfer surfaces. Conversely, if the ACM compressor operates with high values of the pressure ratio, the inlet temperature of the main heat exchanger increases, thus enabling the use of a more compact heat transfer device. However, the pressure drop within the main heat exchanger increases as well, negatively impacting the power consumption of the ram air fan.

Additionally, As the pressure ratio across the ACM compressor increases, the system experiences a rise in entropy production attributable heightened compressor losses. These losses are a direct consequence of the increased pressure ratio, not a result of any variation in compressor efficiency, which remains constant. Consequently, this increase in compressor losses leads to an elevated heat load on the condenser,. This either necessitates a higher ram air mass flow rate, which would result in a higher ram air fan power consumption, or requires a larger condenser, which adds to the system weight causing it to potentially lose its position as an optimal design on the Pareto front.

The power consumption of the VCS compressor is related to the pressure ratio and refrigerant mass flow rate. Figure 5.4b shows the trend of the VCS compressor compression ratio, which decreases as the COP increases. The data points are unevenly distributed, forming two distinct clusters, indicating gaps in the available design configurations for the refrigerant compressor and complicating the optimizer task of identifying viable solutions. The trend observed for the refrigerant compressor pressure ratio is mirrored in the one of the evaporation temperature, as shown in Fig. 5.5c. This temperature decreases until a COP of 0.57, where it abruptly increases by nearly 4 °C. The mass flow rate is linked to the heat load on the evaporator and the vapour quality of the refrigerant entering the evaporator. Lowering the condensation temperature enhances the vapour quality and subsequently decreases the refrigerant mass flow rate. Figure 5.5b shows the trend of decreasing condensation temperature with increasing system COP. Additionally, the heat load is closely associated with the ACM compressor's pressure ratio, illustrated in Figure 5.4c. With an increase in the COP, there is a concurrent decline in both the condensation temperature and ACM compressor pressure ratio, contributing to a reduction in the refrigerant mass flow rate. This decrease, coupled with a reduction in the VCS compressors pressure ratio, accounts for the decreasing power consumption observed in the VCS compressor.

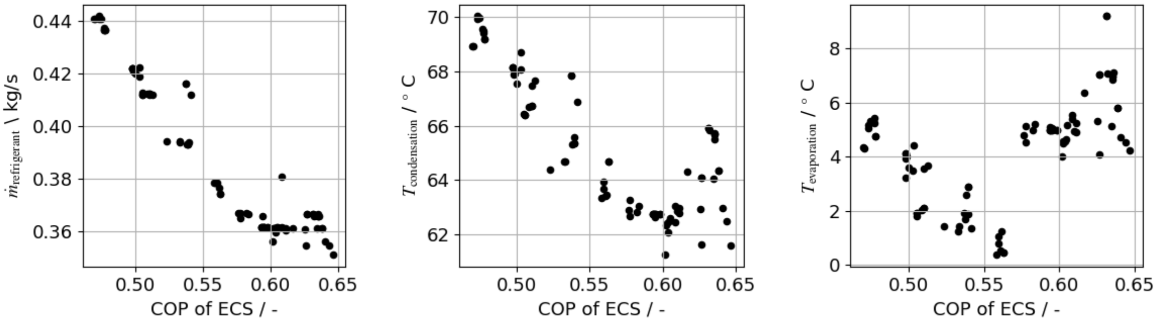

(a) (b) (c)

Figure 5.5: Correlation between Refrigerant mass flow rate (a), condensation temperature (b) and evaporation temperature (c) as a function of the COP.

Finally, the power consumption of the ram air fan is the result of ram air mass flow rate and pressure drops across the condenser and main heat exchanger. Figure 5.6a shows that the ram air mass flow rate varies between 3.2 and 3.5 kg/s for most designs. In correspondence with the highest values of the COP, the ram air mass flow rate drops to approximately 2.6 kg/s. Consequently, the pressure drop on the air side of the condenser and within the main heat exchanger reduces significantly 5.6b. This is attributed to the large dimensions of both the exchangers resulting in correspondence of these designs.

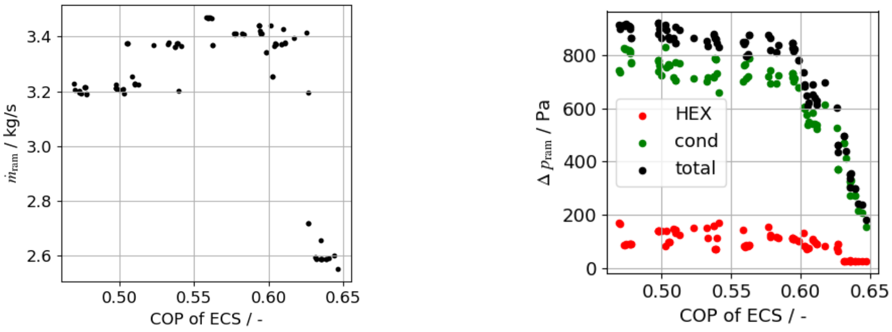

(a) (b)

Figure 5.6: Trend of ACM pressure ratio (a) and total ram air pressure drop (b) as a function of COP.

5.2. HEAT EXCHANGER SIZING

To better understand the distribution of weight within the system, the overall system weight is broken down into its individual components, depicted in Fig. 5.7a. The weight of the main heat exchanger, evaporator and condenser increases with a higher COP, while the heat load on these components reduces, as illustrated in Fig. 5.7b. Among these, the condenser is the heaviest component and it has the highest heat load, as shown in Fig. 5.7b. Although the heat load on the evaporator exceeds that of the main heat exchanger, the evaporator weighs the least. This discrepancy can be explained by the evaporator higher effectiveness, partly attributed to the constant temperature of the refrigerant undergoing a phase change.

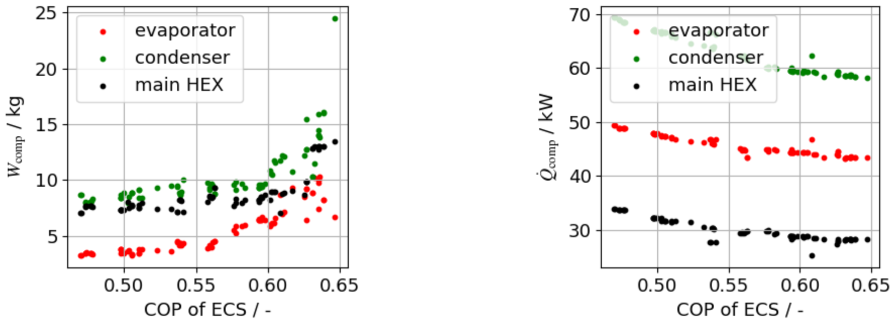

(a) (b)

Figure 5.7: Breakdown of the heat exchangers weight (a) and heat load (b) as a function of COP

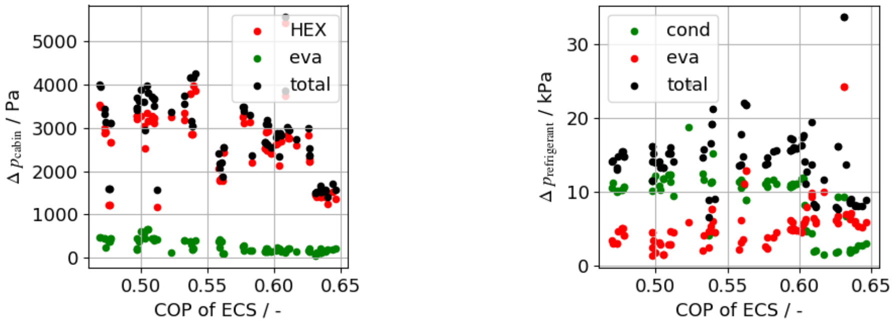

(a) (b)

Figure 5.8: Breakdown of cabin air pressure drop after the main heat exchanger and evaporator (a) and refrigerant pressure drop after the condenser and evaporator as a function of COP

Figures 5.9, 5.10 and 5.11 illustrate the core dimensions of the heat exchangers as a function of the system weight. Figure 5.9 displays the trends of the three core dimensions of the main heat exchanger: width of the cabin air stream inlet area (Fig 5.9a,), height of both fluid streams inlet areas (Fig. 5.9b) and the depth of the ram air stream inlet area (Fig. 5.9c). The variation in width and depth of the main heat exchanger is independent of the system weight. The average width is around about 0.2 m less than the average depth. Given the sixfold higher mass flow rate of the ram air compared to the cabin air, it is justified the large depth of the main heat exchanger depth. Furthermore, Fig. 5.8a shows a significantly larger pressure drop across the cabin air stream as compared to that on the ram air side (Fig 5.6b). This is because the optimizer privileges the reduction of the pressure drop on the ram sir side, since this is directly impacting the ram air fan power demand, and therefore the total electric consumption of the system. The main heat exchanger height increases with system weight (Fig. 5.9b), as a larger height allows for lower pressure drops on both the ram and cabin air sides by increasing both the heat exchanger cross sections and thus by reducing air stream velocities.

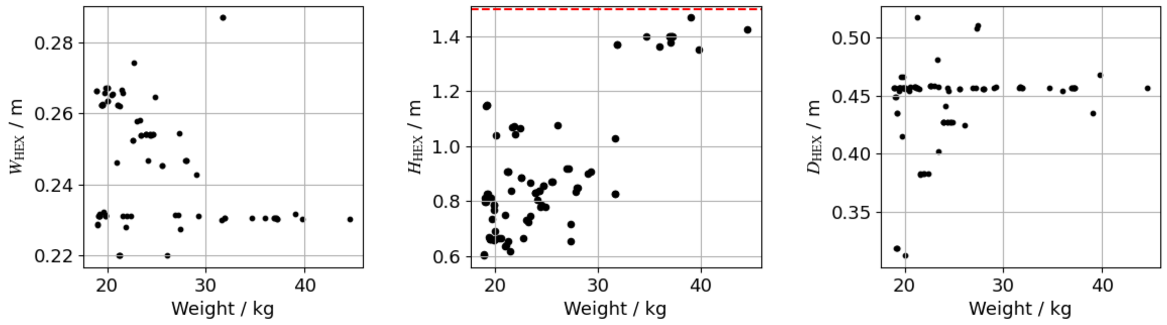

(a) (b) (c)

Figure 5.9: Trend of the core dimensions of the main heat exchanger as a function of the system weight: width of the cabin air side cross-section area (a), height (b) and depth of the ram air side cross-section area (c) .

Figure 5.10 shows the core dimensions of the evaporator as a function of the system weight. The width refers to the cabin air cross section area (Fig. 5.10a), the depth is associated with the refrigerant inlet area (Fig. 5.10c), and the height is the common dimension of both the refrigerant and the air cross sections (Fig. 5.10b). The pressure drop in the cabin air stream attributable to the evaporator is negligible as compared to the pressure drop caused by the main heat exchangers, as demonstrated in Fig. 5.8a. The pressure drop associated with the refrigerant flow is not correlated to the COP of the ECS (Fig. 5.8b). This indicates that the evaporator is not sized to minimize pressure drops, but only to minimize weight at a given set of inlet and outlet conditions. The only dimension of the evaporator which significantly influences the evaporator weight is the height, as illustrated in Fig. 5.10b.

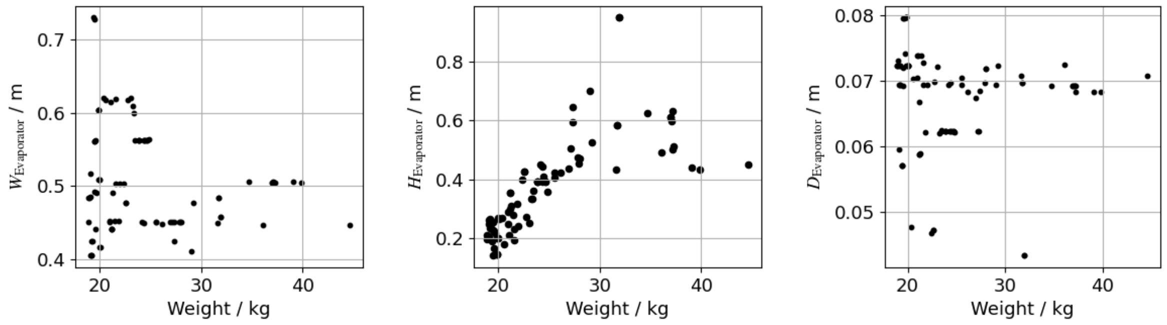

(a) (b) (c)

Figure 5.10: Trend of the core dimensions of the evaporator as a function of the system weight: width of the cabin air side cross section area (a), height (b) and depth of the ram air side cross section area (c).

Figures 5.11a, 5.11b and 5.11c show the variation of the condenser core dimensions: width, height, and depth. In the same fashion as the evaporator, there is not a dependence between the refrigerant stream pressure drop and the system COP. However here it is even clearer, as all solutions approximate the lower condenser depth design bound. The pressure drop on the ram air side is significant as it directly impacts the power consumption of the ram air fan. Figure 5.11a shows an increasing trend of condenser width up to a system weight of 27 kg, indicating a preference for maximizing ram air stream area over the refrigerant area. Beyond a weight of 27 kg, the condenser height also begins to increase.

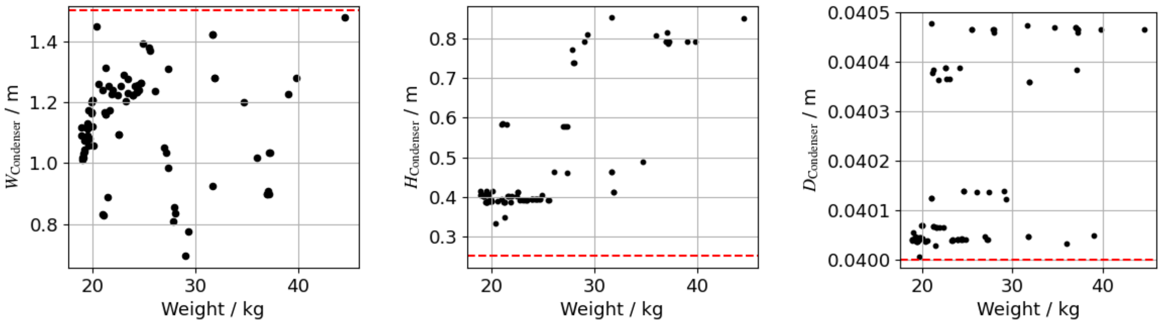

(a) (b) (c)

Figure 5.11: Trends of the core dimensions of the condenser as a function of the system weight: width of the cabin air cross section area (a), height (b) and depth of the ram air cross section area (c).

5.3. REFRIGERANT COMPRESSOR DESIGN

Figure 5.12a illustrates that designs associated with a lower system COP are characterized by refrigerant compressors featuring a higher pressure ratio in the first stage compared to the second stage. A higher pressure ratio for the first stage is favoured since the efficiency of the first stage (Fig. 5.12b) is higher than that of the second stage (Fig. 5.12c). Consequently, a greater relative workload on the first-stage compressor enhances the overall efficiency of the system. In contrast, compressor designs associated with a higher system COP exhibit a decreased pressure ratio in the first stage relative to the second stage. This phenomenon can be attributed to constraints imposed by the optimization of the maximum axial force F_{axial} depicted in Fig. 5.13a. The figure shows that the axial force is high in designs with high first stage pressure ratios, but is reduced in configurations where the first stage pressure ratio is lower than the second stage.

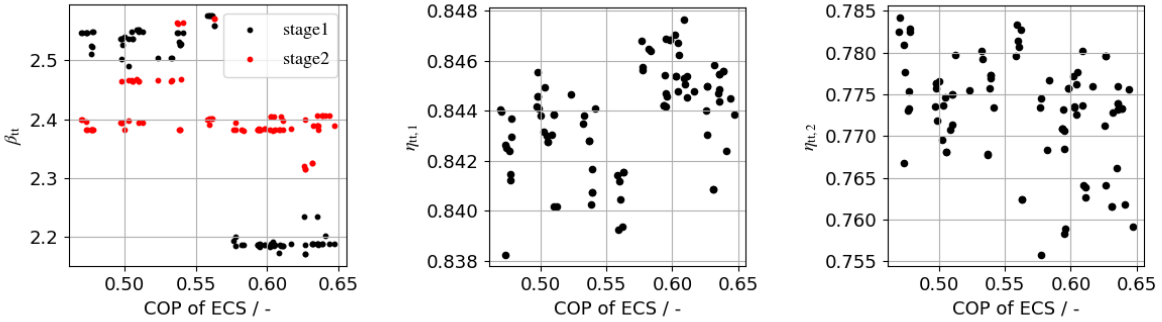

(a) (b) (c)

Figure 5.12: Trends of the refrigerant compressors pressure ratio (a) and total efficiency of the first (b) and second (c) stage compressor as a function of the system COP

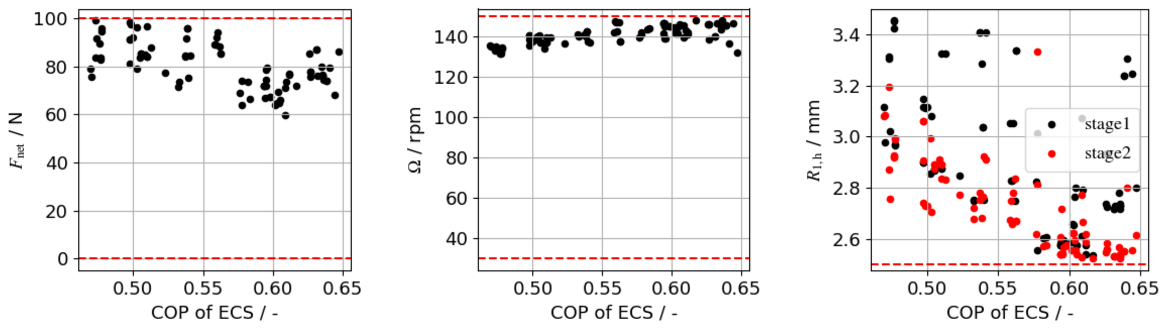

(a) (b) (c)

Figure 5.13: Trends of the refrigerant compressors axial force (a), rotational speed (b) and impeller hub radius (c) as a function of the system COP

No trend between the compressor input variables and the objective variables of the optimization problem can be identified. However, there is a difference between the set of input variables for each compressor stage. Table 5.1 shows the average values of the input for the first and the second stages of the refrigerant compressor. The average value of the swallowing capacity ϕ_{t1} is an indicator of the flow capacity of the stage, and it is higher for the first stage than for the second one. This is expected as the flow entering the second compressor is at a higher pressure, and thus at a lower density for the same mass flow rate as the first stage compressor. Therefore, the volumetric flow rate of the second stage is lower than the first one, thus leading to a more compact design of the impeller wheel. The average value of the load coefficient ψ is 0.84. The load coefficient is the ratio between the specific work of the stage and the blade speed at the outlet of the impeller. Since the total enthalpy difference of the stage depends on both the pressure ratio and α_2, the load coefficient influences the rotational speed of the compressor. The design rotational speed, displayed in Fig. 5.13b, is approximately equal to 145 krpm, which is close to the maximum allowable value imposed in the optimization constraint. α_2 is the absolute flow angle at the inlet of the diffuser. α_2 of the second stage compressor is smaller, which relates to a higher backsweep angle. For smaller compressors a higher α_2 is expected, as this reduces the meridional velocity component, which increases the outlet blade span and decreases effect of losses due to a relatively high tip clearance. However, a higher backsweep angle requires an higher rotational speed for the same amount of work. As all of the compressor designs approach the rotational speed constraint, this likely imposes a limit on the maximum value of α_2 and explains the lower value of α_2 for the second stage compressor. k is the shape factor and indicates the ratio between the impeller inlet hub and shroud radius ratio. The second stage has a smaller shape factor, meaning that the ratio of the hub radius and shroud radius $R_{1,h}/R_{1,s}$ is larger for the second stage. Thus a smaller shape factor k means that the difference between the hub and shroud radius is relatively smaller. The reduced size of the second stage is a results of the lower volumetric flow rate. Figure 5.13c illustrates the dimensions of the impeller radius at the hub for both stages. The design of the second stage impeller is constrained by the minimum hub radius optimization constraint. This constraint necessitates an increase in the optimal value of the impeller hub radius $R_{1,h}$. Consequently, the impeller shroud radius $R_{1,s}$ must also increase to maintain the necessary inlet area. However, the increase in $R_{1,s}$ is less significant because the inlet area is proportional to the square of the radius. Therefore, the constraint imposed by $R_{1,h}$ results in a smaller shape factor for the second stage impeller.

Table 5.1: Set of average optimal input parameters of the compressor.

Parameter	Symbol	Value	Unit
Swallowing capacity [-]	ϕ_{t1}	0.176	0.072
Loading coefficient [-]	ψ	0.84	-
Absolute outlet angle [°]	α_2	73	69
Diffuser radius ratio [-]	$\frac{R3}{R2}$	1.47	1.46
Shape factor [-]	κ	0.91	0.86

5.4. OPTIMAL DESIGN FOR MINIMAL FUEL CONSUMPTION

The methodology selected to relate the ECS power consumption and weight to the aircraft fuel consumption is described in Ch. 4.4.1. This method accounts for both the power consumption of the ECS on the ground operation and the aircraft weight during flight operation. The optimal design is dependent on the mission profile, shown in Fig. 4.3. The analysis enables the identification of an optimal design point that minimises the total fuel consumption during the entire flight mission, and it is indicated with a yellow marker in Fig. 5.14. A design with relatively high weight and low power consumption is favoured.

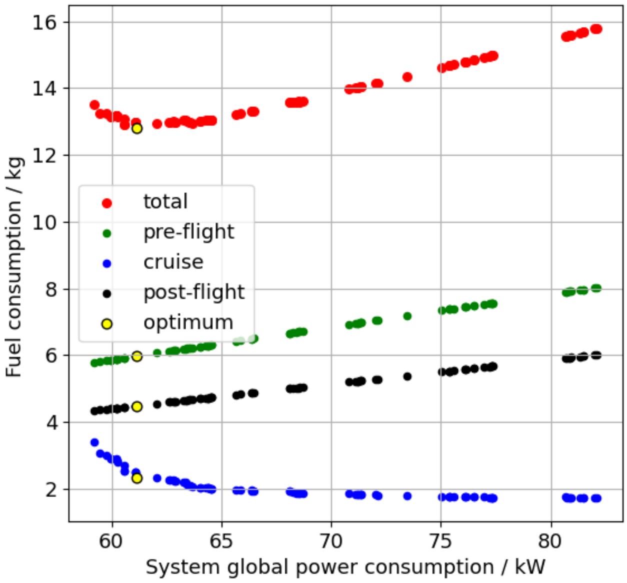

Figure 5.14: Fuel consumption as a function of the total power demand of the ECS.

The results for this optimal design are displayed in Tab. 5.2. Note that only the evaporator, condenser and main heat exchanger are included in the system weight.

Table 5.2: Optimal design point corresponding to the minimum fuel consumption of the ECS at ground conditions.

Metric	Value	Unit
P_{el}	61.2	kW
Weight	29.3	kg
T_{cond}	61.2	°C
T_{eva}	8.2	°C

Fig. 5.15 shows the thermodynamic processes undergone by the cabin air in the $T-s$ chart in correspondence of the optimal design point. A reference line is drawn to indicate the ambient temperature. The effect of coupling a VCC to the ACM becomes visible when looking at the outlet temperature of the evaporator, S5 in Fig. 5.15, which is lower than the ambient temperature. Thus the use of the VCC lowers the required pressure ratio of the ACM compressor. Fig. 5.15 also shows that the turbine has a large entropy production for its relatively limited power output (thermodynamic process S6-S7). This increases the heat load on the heat exchangers (SX-SX) and decreases the efficiency of the ACM.

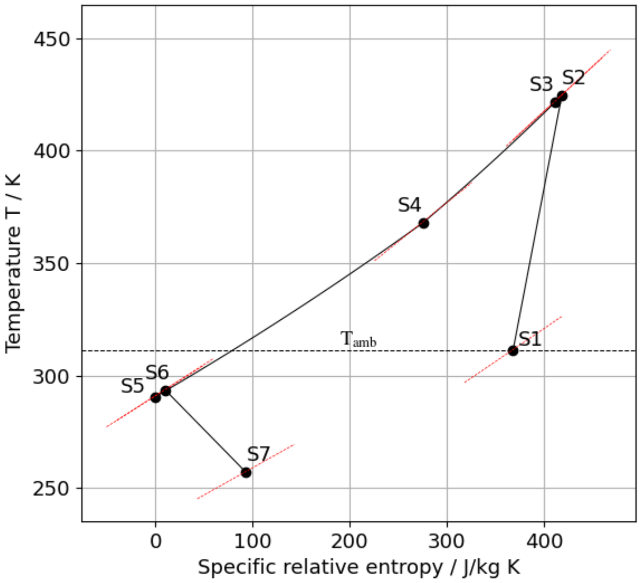

Figure 5.15: $T-s$ thermodynamic chart indicating the processes undergone by the cabin air for the optimal ECS design in the case of ground conditions.

Figure 5.16 illustrates the $T-s$ thermodynamic chart with the processes undergone by the refrigerant within the VCC loop. The effect of the ACM and VCC coupling becomes evident: the temperature at the inlet of the cabin air evaporator significantly exceeds that of the ram ambient air. Additionally, the cabin air outlet temperature of the evaporator is higher than the required cabin mixing manifold temperature due to the inclusion of the ACM. This high temperature difference facilitates the design of a more compact and thus lighter evaporator. Moreover, the higher outlet temperature allows for a higher evaporation temperature, thereby reducing the compression ratio required of the refrigerant compressor.

Figure 5.16: Thermodynamic cycle showing the refrigerant stream

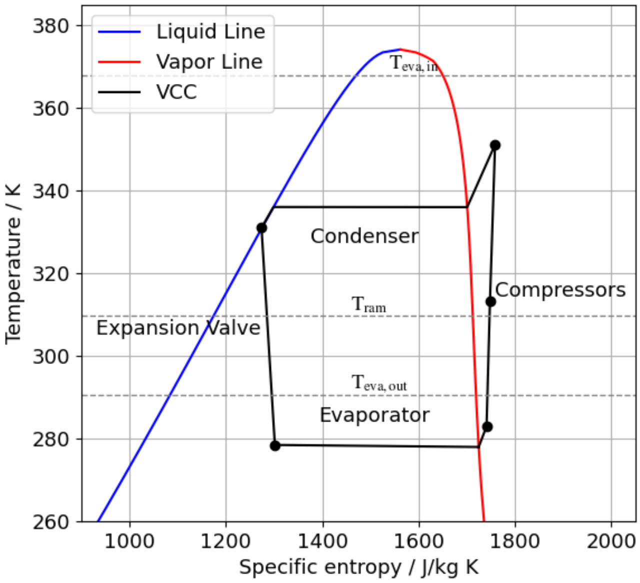

5.5. PERFORMANCE AT CRUISE

The system is sized to operate during a hot day at ground conditions. In the case of the ECS operating at cruise conditions, there are three main aspects to account with respect to the case at ground conditions: i) the ram air heat sink is significantly colder and it is equal to -56.5°C, ii) the environmental air must be pressurized by a factor of 3.88 to meet the cabin air pressure requirements, and iii) the ACM turbine is bypassed. These different operating conditions have an influence on the operation of the VCS, therefore it is necessary to verify whether the ECS sized to operate at ground conditions can also allow for the operation at cruise conditions. In the case of aircraft flying at cruise, the VCS operates with a different condensation temperature, evaporation temperature and refrigerant mass flow rate. Despite the fact that the temperature of the air delivered by the ECS is lower at cruise conditions, the absence of the turbine downstream of the evaporator leads the system to operate at a lower evaporation temperature. At the same time, the condensation temperature also decreases because of the lower ram air temperature. The operating conditions of the ECS at cruise conditions are listed in Tab. 5.3.

Metric	Value	Unit
PR 1st stage	1.6	-
PR 2nd stage	1.7	-
$\mathrm{P}_{\mathrm{compressor,cab}}$	66.1	kW
$\mathrm{P}_{\mathrm{compressors,ref}}$	5.3	kW
Weight	29.3	kg
$\mathrm{T}_{\mathrm{cond}}$	20.8	°C
$\mathrm{T}_{\mathrm{eva}}$	-8.1	°C
$\dot{\mathrm{m}}_{\mathrm{ram}}$	0.725	kg/s

Table 5.3: Operating conditions and system performance of the ECS operating at cruise conditions.

The performance analysis of the system during cruise conditions is simplified by omitting the design of the refrigerant compressor. The high compression ratio of the cabin air compressor results in a substantial temperature differential between the cabin air stream and the ram air stream. This, combined with the relatively high temperature of the cabin air mixing manifold, imposes a higher heat load on the primary heat exchanger compared to ground conditions. Consequently, this lowers the heat load on the evaporator and reduces the refrigerant mass flow rate. Furthermore, a reduced condensation temperature improves the vapour quality and further decreases the refrigerant mass flow rate. The compressor is engineered to accommodate a specific volumetric flow rate. The reduced mass flow rate, which accounts for the effects of temperature and pressure variations, is expressed as follows

$$\dot{m}_{\text{red}} = \frac{\dot{m} \cdot \sqrt{T_{\text{in}}}}{P_{\text{in}}} \tag{5.2}$$

While the temperature increase does reduce the reduced mass flow rate, the impact of the pressure of the refrigerant at the refrigerant is more pronounced and leads to a higher reduced mass flow rate. All these factors—variations in mass flow rate, evaporation pressure and temperature—collectively affect the volumetric flow rate through the compressor. Therefore, it is imperative to consider the compressor design during the optimization phase of cruise operations.

6

CONCLUSION

Aviation contributes significantly to anthropogenic climate forcing, with 3.5% of the total net anthropogenic effective radiative force in 2011 [11]. The contribution of aviation has only grown since. Among the various systems within an aircraft, the Environmental Control System (ECS) stands out as the largest consumer of non-propulsive enenergy, accounting for 3-5% of an aircraft total energy consumption [14]. As the aviation industry moves towards electrification, driven by initiatives like the European Union's "Fly the Green Deal" [13], there is a critical need for innovative more efficient ECS architectures. This thesis showed a novel hybrid ECS design that includes features from both the air cycle machine (ACM) and he vapor compression cycle (VCC). The research question considered in this thesis is

- **What is the optimal design of an electrically driven environmental control system operating on a hot humid day with features of both an air cycle machine and vapour compression cycle?**

To address the posed research question and sub-questions stated in chapter 1, this study implements an integrated design method that simultaneously optimizes the thermodynamic cycle, high-speed radial refrigerant compressor and heat exchanger components to minimize power consumption and weight of the ECS operating on the ground during a hot and humid day at 38 °C. This method was implemented through an integration of a Modelica a-causal model, an in-house compressor design tool [8] and a Python-implemented genetic optimization algorithm. The optimization results facilitated the selection of an optimal design based on a typical single-aisle aircraft flight mission. The performance of this design was evaluated at cruise conditions, as well. The answer to the aforementioned research question is

- **The design of a hybrid ECS is feasible. The hybrid configuration shows potential as an efficient solution for cabin air cooling. The study successfully identified the Pareto front of the optimal hybrid ECS solutions. The power consumption ranges from 59 kW to 82 kW per pack, suggesting a lower power consumption than a VCC-based ECS. The ECS weight ranges from 19 kg to 45 kg. The results indicated that any reduction in power consumption results in an increase in system weight.**

Additionally, the following conclusions can be drawn from this study

1. The condenser imposes the highest pressure drop in the ram air stream. Thus, the sizing of the condenser is critical to limit the power consumption of the ram air fan;
2. The design space for the hybrid ECS was notably constrained by the capabilities of the high-speed radial refrigerant compressor. Integrating the refrigerant compressor design is crucial as the VCC operating parameters influence component sizing and the overall ECS power consumption;
3. An optimal solution for a typical flight mission of 1.8 h is identified. This design has a power consumption of 61.2 kW and a total weight of 29.3 kg;
4. The heat exchangers designed for the case of ground operating meet the requirements of the ECS in the case of cruise conditions. However, this analysis is limited since the preliminary design of the centrifugal compressor was overlooked.

6.1. LIMITATIONS AND RECOMMENDATIONS

The limitations highlighted during this research and future recommendations are stated.

1. The optimization was performed at ground conditions, which does not account for the impact of drag or accurately reflect the operational demands during cruise conditions. Consequently, it is imperative to perform a multi-point optimization that includes cruise conditions to ensure that the ECS operates efficiently across all flight phases.

2. The selection of R134A as working fluid for the VCC loop has an impact on both the thermodynamic performance of the system and the design of its main components. Therefore, the optimization framework should also account for the effect of alternative refrigerants.

3. The stiffness of the complex Modelica model of the ECS compromises the robustness of the solution, resulting in slow convergence of the Pareto front and high computational costs. To improve these aspects, simplification of the model and minimizing the number of design variables are recommended. Furthermore, it is advised to conduct a sensitivity analysis to properly select the design variables which significantly influence the objective functions of the optimization problem.

BIBLIOGRAPHY

[1] M. Merzvinskas, C. Bringhenti, J. Tomita, and C. de Andrade, *Air conditioning systems for aeronautical applications: a review,* The Aeronautical Journal **124**, 499 (2020).

[2] C. Müller and D. Scholz, *The Vapor Compression Cycle in Aircraft Air-Conditioning Systems*, Tech. Rep. (Hamburg University of Applied Sciences, 2017).

[3] *D. Vapor Cycle Systems,* .

[4] S. Golle, U. Hesse, E. Klausner, M. Raddatz, F. Klimpel, and H. Brunswig, *Betriebsphasenabhängig steuerbare Flugzeugklimaanlage und Verfahren zum Betreiben einerderartigen Flugzeugklimaanlage,* (2015).

[5] D. P. Sekulic and R. K. Shah, *Fundamentals of Heat Exchanger Design*, 2nd ed. (Wiley, 2023) pp. 6–6.

[6] F. Ascione, P. Colonna, and C. De Servi, *Integrated design optimization method for novel vapour-compression-cycle-based environmental control systems,* Applied Thermal Engineering **236**, 121261 (2024).

[7] D. Rusch and M. Casey, *The Design Space Boundaries for High Flow Capacity Centrifugal Compressors,* Journal of Turbomachinery **135** (2013), 10.1115/1.4007548.

[8] A. Giuffre, P. Colonna, and M. Pini, *The Effect of Size and Working Fluid on the Multi-Objective Design of High-Speed Centrifugal Compressors,* International Journal of Refrigeration **143**, 43 (2022).

[9] A. Giuffre', P. Colonna, and M. Pini, *Design Optimization of a High-Speed Twin-Stage Compressor for Next-Gen Aircraft Environmental Control System,* Journal of Engineering for Gas Turbines and Power **145** (2023), 10.1115/1.4056022.

[10] A. Giuffre', P. Colonna, and C. De Servi, *Dynamic thermal model of passenger aircraft for the estimation of the cabin cooling and heating requirements,* Applied Thermal Engineering **244**, 122641 (2024).

[11] D. Lee, D. Fahey, A. Skowron, M. Allen, U. Burkhardt, Q. Chen, S. Doherty, S. Freeman, P. Forster, J. Fuglestvedt, A. Gettelman, R. De León, L. Lim, M. Lund, R. Millar, B. Owen, J. Penner, G. Pitari, M. Prather, R. Sausen, and L. Wilcox, *The contribution of global aviation to anthropogenic climate forcing for 2000 to 2018,* Atmospheric Environment **244**, 117834 (2021).

[12] A. K. Sehra and W. Whitlow, *Propulsion and power for 21st century aviation,* Progress in Aerospace Sciences **40**, 199 (2004).

[13] Advisory Council for Aviation Research and Innovation in Europe (ACARE), *the Green Deal Europe's Vision for Sustainable Aviation Report of the Advisory Council for Aviation Research and Innovation in Europe (ACARE) Fly*, Tech. Rep. (European Union, 2022).

[14] D. Bender, *Exergy-Based Analysis of Aircraft Environmental Control Systems and its Integration into Model-Based Design vorgelegt von Diplom-Ingenieur*, Ph.D. thesis, Technischen Universität Berlin, Berlin (2019).

[15] K. Linnett and R. Crabtree, *JOURNAL OF AEROSPACE*, Tech. Rep. (1993).

[16] M. Sinnet, *787 No-Bleed Systems: Enhancing Fuel and Enhancing Operational Efficiencies,* Aero magazine Q4 , 06 (2007).

[17] C. P. Arora, *Refrigeration and Air Conditioning* (Tata McGraw-Hill, 2000).

[18] W. C. Reynolds and P. Colonna, *Thermodynamics: Fundamentals and engineering applications* (Cambridge University Press, 2018).

[19] R. Slingerland and S. Zandstra, *Bleed Air versus Electric Power Off-takes from a Turbofan Gas Turbine over the Flight Cycle,* in *7th AIAA ATIO Conf, 2nd CEIAT Int'l Conf on Innov and Integr in Aero Sciences,17th LTA Systems Tech Conf; followed by 2nd TEOS Forum* (American Institute of Aeronautics and Astronautics, Reston, Virigina, 2007).

[20] V. Cavalcanti and C. Andrade, *A Trade-off Study of a Bleedless and a Conventional Air Conditioning Systems,* in *XVII Congresso e Exposição Internacionais da Tecnologia da Mobilidade* (Sao Paulo, 2008) pp. 2008–36.

[21] L. Faleiro, *Summary of the European Power Optimised Aircraft (POA) Project,* in *International Congres of the Aeronautical Sciences (ICAS)* (2006).

[22] B. Rebbechi, *A REVIEW OF AIRCRAFT CABIN CONDITIONING FOR OPERATIONS IN AUSTRALIA*, Tech. Rep. (DEPARTMENT OF DEFENCE DEFENCE SCIENCE AND TECHNOLOGY ORGANISATION AERONAUTICAL RESEARCH LABORATORIES, 1980).

[23] United States Enironmental Protection Agency, *Phasing Out HCFC Refrigerants To Protect The Ozone Layer (EPA-430-F-09-080),* (2015).

[24] C. R. Holt, *The Turbo Commander Bleed Air Environmental System,* (1969).

[25] D. Scholz, *Aircraft Cabin Air and Engine Oil - A Systems Engineering View.* (2017).

[26] G. K. Payne, *Air-Cycle Air Conditioning of Turbine-Powered General Aviation and Commuter Aircraft,* (1985).

[27] A. Puntel, S. Emo, T. E. Michalak, J. Ervin, L. Byrd, V. Tsao, and T. Reitz, *Refrigerant Charge Management and Control for Next-Generation Aircraft Vapor Compression Systems,* (2013).

[28] H. Hu, H. Sun, C. Wu, X. Wang, and Z. Lv, *A steady-state simulation model of supplemental cooling system integrated with vapor compression refrigeration cycles for commercial airplane,* Applied Thermal Engineering **166**, 114692 (2020).

[29] H. Saito, S. Uryu, N. Takahashi, N. Morioka, and H. Oyori, *Study of VCS Design for Energy Optimization of Non-Bleed Electric Aircraft,* (2014).

[30] Clean Sky 2 JU, *A breath of fresh air with Clean Sky's Environmental Control System,* Cleansky.eu (2021).

[31] P. D. V. Mahindru, P. Mahendru, and D. V. Mahindru, *Global Journal of researches in engineering: d AEROSPACE Engineering Environmental Control System for Military & Civil Aircraft Environmental Control System for Military Civil Aircraft Environmental Control System for Military & Civil Aircraft,* (2011).

[32] R. Agrawal and S. Mada, *Hybrid Environmental Control System for Military Aircraft Hybrid Environmental Control System for Military Aircraft Hybrid Environmental Control System for Military Aircraft,* (2013).

[33] A. Genty, A. Saunders, J. P. Cimino, and S. Rose, *Environmental Control System for Light Turbo Prop,* (2003).

[34] Dassault Systèmes, *Dymola 2022x,* (2021).

[35] B. J. McBride, M. J. Zehe, and S. Gordon, *NASA Glenn Coefficients for Calculating Thermodynamic Properties of Individual Species*, Tech. Rep. (NASA Glenn Research Center Cleveland, Cleveland, 2002).

[36] R. Tillner-Roth and H. D. Baehr, *An International Standard Formulation for the Thermodynamic Properties of 1,1,1,2-Tetrafluoroethane (HFC-134a) for Temperatures from 170 K to 455 K and Pressures up to 70 MPa,* Journal of Physical and Chemical Reference Data **23**, 657 (1994).

[37] I. H. Bell, J. Wronski, S. Quoilin, and V. Lemort, *Pure and Pseudo-pure Fluid Thermophysical Property Evaluation and the Open-Source Thermophysical Property Library CoolProp,* Industrial & Engineering Chemistry Research **53**, 2498 (2014).

[38] J. Holman, *Heat Transfer*, 10th ed. (McGraw-Hill, New York, 2010) pp. 546–546.

[39] S. L. Dixon and C. A. Hall, *Fluid Mechanics and Thermodynamics of Turbomachinery*, sixth ed. (Elsevier Inc., 2010).

[40] K. Deb, A. Pratap, S. Agarwal, and T. Meyarivan, *A fast and elitist multiobjective genetic algorithm: NSGA-II,* IEEE Transactions on Evolutionary Computation **6**, 182 (2002).

[41] D. Scholz, *DOC SYS-A Method to Evaluate Aircraft Systems*, Tech. Rep. (Deutsche Gesellschaft für Luft- und Raumfahrt, Bonn, 1998).

[42] IATA Consulting, *HKIA long-term traffic and emission forecast*, Tech. Rep. (IATA, 2014).

[43] Pratt & Whitney, *Auxiliary Power Units (APU),* .

[44] M. Schmidt, *A review of aircraft turnaround operations and simulations,* Progress in Aerospace Sciences **92**, 25 (2017).

[45] W. Vankan and W. Lammen, *Parallel hybrid electric propulsion architecture for single aisle aircraft - powertrain investigation*, Tech. Rep. (NLR-Netherlands Aerospace Centre, 2019).